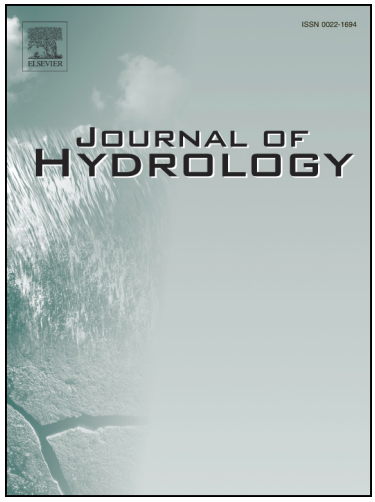

Resistivity and self-potential tomography applied to groundwater remediation and contaminant plumes: Sandbox and field experiments

D. Mao, A. Revil, R.D. Hort, J. Munakata-Marr, E.A. Atekwana, B. Kulessa

PII: S0022-1694(15)00714-3
DOI: http://dx.doi.org/10.1016/j.jhydrol.2015.09.031
Reference: HYDROL 20722

To appear in: *Journal of Hydrology*

Received Date: 21 May 2015
Revised Date: 9 September 2015
Accepted Date: 11 September 2015

Please cite this article as: Mao, D., Revil, A., Hort, R.D., Munakata-Marr, J., Atekwana, E.A., Kulessa, B., Resistivity and self-potential tomography applied to groundwater remediation and contaminant plumes: Sandbox and field experiments, *Journal of Hydrology* (2015), doi: http://dx.doi.org/10.1016/j.jhydrol.2015.09.031

Resistivity and self-potential tomography applied to groundwater remediation and contaminant plumes: sandbox and field experiments

D. Mao (1), A. Revil (1, 2), R. D. Hort (3), J. Munakata-Marr (3),

E. A. Atekwana (4) and B. Kulessa (5)

(1) Colorado School of Mines, Dept. of Geophysics, Green Center, 1500 Illinois St., Golden, CO 80401, USA.

(2) ISTerre, CNRS, UMR CNRS 5275, Université Savoie Mont-Blanc, 73376 cedex, Le Bourget du Lac, France.

(3) Colorado School of Mines, Dept. of Civil and Env. Engineering, 1500 Illinois St., Golden, CO 80401, USA.

(4) Boone Pickens School of Geology, Oklahoma State University, Stillwater, OK 74075, USA.

(5) College of Science, Swansea University, Singleton Park, Swansea, SA2 8PP, Wales, UK

Short Title: SP/resistivity tomography

Corresponding author: André Revil (arevil@mines.edu)

Emails of the authors: arevil@mines.edu; maodeqiang@gmail.com; junko@mines.edu; estella.atekwana@okstate.edu; ryan.d.hort@gmail.com; b.kulessa@swansea.ac.uk

Intended to be published in Journal of Hydrology

Abstract. Geophysical methods can be used to remotely characterize contaminated sites and monitor in situ enhanced remediation processes. We have conducted one sandbox experiment and one contaminated field investigation to show the robustness of electrical resistivity tomography and self-potential (SP) tomography for these applications. In the sandbox experiment, we injected permanganate in a trichloroethylene (TCE)-contaminated environment under a constant hydraulic gradient. Inverted resistivity tomograms are able to track the evolution of the permanganate plume in agreement with visual observations made on the side of the tank. Self-potential measurements were also performed at the surface of the sandbox using non-polarizing Ag-AgCl electrodes. These data were inverted to obtain the source density distribution with and without the resistivity information. A compact horizontal dipole source located at the front of the plume was obtained from the inversion of these self-potential data. This current dipole may be related to the redox reaction occurring between TCE and permanganate and the strong concentration gradient at the front of the plume. We demonstrate that time-lapse self-potential signals can be used to track the kinetics of an advecting oxidizer plume with acceptable accuracy and, if needed, in real time, but are unable to completely resolve the shape of the plume. In the field investigation, a 3D resistivity tomography is used to characterize an organic contaminant plume (resistive domain) and an overlying zone of solid waste materials (conductive domain). After removing the influence of the streaming potential, the identified source current density had a magnitude of 0.5 A m^{-2}. The strong source current density may be attributed to charge movement between the neighboring zones that encourage abiotic and microbially enhanced reduction and oxidation reactions. In both cases, the self-potential source current density is located in the area of strong resistivity gradient.

1. Introduction

In characterizing contaminated groundwater sites, in situ measurements gathered only from wells are generally insufficient for tracking plume migration and to characterize concentration changes beyond the immediate area adjacent to the well. Aquifer heterogeneity can cause localized flow paths that may not be easily detected from monitoring well samples only. There is a therefore a growing interest in hydrogeophysics in developing methods for monitoring groundwater remediation that would complement well data. Geophysical methods can be employed to characterize contaminant plumes (e.g., Clement et al., 1997; Gao et al., 2007; Castro and Branco, 2003), to visualize preferential flow paths (e.g., Kulessa et al., 2003; Ikard et al., 2012; Jardani et al., 2013), and to detect and to monitor chemical species injected in the subsurface for remediation (e.g., Hubbard et al., 2001; Gehman et al., 2009; Williams et al., 2009).

Electrical resistivity tomography (ERT) is a well-established geophysical method that has been widely used to investigate the variations in electrical conductivity associated with changes in pore water ionic strength or water phase saturation (e.g., Slater, 2007; Loke et al., 2013). During an ERT survey, electrical current is injected through electrodes (called current electrodes), and, at the same time, electrical potentials are measured at other electrodes (called potential electrodes). Resistance or apparent resistivity data can be obtained through electrode arrays located at the ground surface and in vertical or horizontal boreholes as documented in various field studies (Daily and Ramirez, 1995; Slater et al., 2000; Kemna et al., 2002). The use of multichannel resistivity meters has decreased the time required to take a single snapshot. These surveys can be repeated at different time periods to track the movement of an injected chemical solution. Time-lapse inversions can then be also performed (LaBrecque and Yang,

2001; Kim et al., 2009; Karaoulis et al., 2014) and applied to track the concentration changes over time (e.g., Singha and Gorelick, 2005; Cassiani et al., 2006; Revil et al., 2013) and also dense non-aqueous phase liquid plumes (Power et al., 2015). The drawback of the method is that it takes usually some time to perform a resistivity acquisition (i.e., getting a single snapshot), and the interpretation of resistivity tomograms is not easy. Indeed, electrical resistivity of porous rocks depends on both the bulk conductivity associated with conduction in the pore network and surface conduction in the electrical double layer coating the surface of the grains (Revil, 2013a, b). We note a worrying tendency in the recent hydrogeophysics literature to oversell what electrical resistivity alone can accomplish by using Archie's law and neglecting the effect of surface conductivity (for instance Comina et al., 2010, 2011).

A less-known and less-used geophysical method is the self-potential method. In contrast to electrical resistivity, the self-potential method is a passive technique. Electrical fields resulting from the existence of source currents in the conductive subsurface are measured in a way that is very similar to electroencephalography in medical imaging (Trujillo-Barreto et al., 2004). In the case of contaminant plumes, the current density is generated by the presence of the plume itself. Indeed, charge carrier concentration gradients generate a source current density known as a diffusion current (e.g., Maineult et al., 2004, 2005, 2006; Revil et al., 2009; Martinez-Pagan et al., 2010). The resulting electrical field is called the diffusion or membrane potential. Self-potential signals of this type have been recently used to measure the velocity of injected saline pulses moving through dam and embankment leaks both in laboratory and field conditions (Ikard et al., 2012).

One of the drawbacks of the self-potential method is the existence of several source current densities in field conditions. Indeed, three other mechanisms can generate in situ source

current densities. One is called the streaming current and is related to the flow of the pore water dragging part of the electrical diffuse layer coating the surface of the grains (e.g., Revil et al., 2002; Suski et al., 2004; Rizzo et al., 2004 and Titov et al., 2005). A second (and generally corresponding to a relatively small effect) is the thermoelectric effect related to temperature influences upon the chemical potential of the charge carriers (Leinov et al., 2010; Ikard and Revil; 2014; Karaoulis et al., 2014). Finally, a current density is generally associated with a gradient in the redox potential in the presence of electronic conductors such as ore bodies or certain microorganisms (e.g., Naudet et al., 2004; Castermant et al., 2008; Risgaard-Petersen et al., 2012). We have developed, however, methodologies to separate various contributions as explained for instance in Naudet et al. (2004).

Self-potential measurements are especially interesting for the purpose of measuring plume advection because of the speed at which they could potentially be used. Since self-potential is a passive approach, changes can be observed in real time, which is a real advantage of the method with respect to ERT as explained in Ikard et al. (2012). Getting a snapshot of self-potential data and inverting it can be an instantaneous process in the field. An additional advantage is that, in contrast to ERT, the inversion of self-potential signals is a linear problem since the data (the self-potential signals) are linearly related to the source current density corresponding to the model parameter. Therefore, the inverse problem can be solved very quickly, possibly in a single iteration if the regularization coefficient has been predetermined using simulations done prior to the measurements. This speed advantage would be especially relevant for developing automated monitoring systems for contaminant plume remediation and for following advective saline tracers through preferential flow paths. This can be advantageous in field conditions to make decisions in real time, for instance regarding addition of chemical or

biological remediation amendments. Resistivity measurements take more time partly due to the lack of equipment able to inject various sources of current at different frequencies simultaneously and having massive multichannel capabilities for the voltage electrodes. In addition, the inversion of resistance data is a non-linear problem, requiring more time for inversion.

In principle, the inversion of self-potential data requires resistivity data for the computation of the kernel. That said, self-potential tomography can be done without resistivity information or by using resistivity information from auxiliary data like in electroencephalography (see Trujillo-Barreto et al., 2004) and during localization of hydromechanical disturbances (see Revil et al., 2015). In addition, self-potential and resistivity tomography can be considered as complementary techniques in identifying and monitoring contaminant plumes and their remediation.

In this study, we investigate the use of both ERT and self-potential surveys to monitor the movement of permanganate in a TCE-contaminated sandbox and to characterize a contaminated groundwater site at an abandoned gas factory. The purpose of the sandbox experiment is to study the possibility of using these two methods to evaluate the evolution of a plume in the shallow subsurface. While ERT is a well-established technique, very few experiments have used time-lapse self-potential signals to monitor remediation of a contaminant plume and for which the inversion results can be compared to the ground truth. For the field experiment, we use these two methods to locate the contaminant and source current density.

2. Methods

In this section, we introduce the simulation techniques employed in this research. Forward and inverse modeling methods are addressed for both resistivity and self-potential tomography.

2.1. Forward Modeling

2.1.1. Electrical resistivity

The voltage response due to a known DC current during an ERT survey is described by the following elliptic equation:

$$\nabla \cdot (-\sigma \nabla \psi) = \mathrm{I}\left(\delta(\mathbf{r}-\mathbf{r}_{s^+}) - \delta(\mathbf{r}-\mathbf{r}_{s^-})\right), \tag{1}$$

where ψ denotes the electrical potential (in V), σ is the electrical conductivity (in S m^{-1}), I is the injected current magnitude (in A), $\mathbf{r}_{s^+}$ and $\mathbf{r}_{s^-}$ are the position vectors of the injection and retrieving electrodes A and B, and δ denotes the Dirac (delta) functions (in m^{-3}). Two types of boundary conditions can be used:

$$\begin{cases} \psi\big|_{\partial\Omega_1} = 0 \\ \sigma \dfrac{\partial \psi}{\partial \mathbf{n}}\bigg|_{\partial\Omega_2} = 0 \end{cases}. \tag{2}$$

The boundary $\partial\Omega_1$ indicates ground condition (prescribed potential value) while $\partial\Omega_2$ corresponds to an insulating boundary (**n** is the unit vector normal to this boundary). In the sandbox experiment, the forward model will consider the effect of the insulating boundary at each wall of the sandbox. In field conditions, the ground surface is considered an insulating boundary, and the potential goes to zero at infinity in the ground. In the following, the current flow is solved as a 3D problem.

2.1.2. Self-potential

In a self-potential survey, the source current density is generated inside the conductive material. The total current density **J** (in A m^{-2}) in the sandbox is described by a generalized Ohm's law

$$\mathbf{J} = \sigma\mathbf{E} + \mathbf{J}_s, \tag{3}$$

where **E** is the electrical field (in V m-1), and $\mathbf{J}_s$ is the source current density that is responsible for the observed electrical field (in A m^{-2}). Since the time-variations of the current density are very slow, we can use the quasi-static limit of the Maxwell equations for which $\nabla \times \mathbf{E} = 0$, and therefore $\mathbf{E} = -\nabla\psi$, ψ being the self-potential field. In this limit, the conservation of charge takes the form

$$\nabla \cdot \mathbf{J} = 0. \tag{4}$$

Combining equations (3) and (4), the scalar potential is the solution of a Poisson equation,

$$\nabla \cdot (\sigma \nabla \psi) = \nabla \cdot \mathbf{J}_s. \tag{5}$$

The boundary conditions have the same form as indicated by equation (2) for the resistivity problem. All the boundaries of the sandbox will be considered as insulating boundaries, while for the field case, only the ground surface is considered to be an insulating boundary. According to equation (5), the self-potential field is affected by the electrical conductivity distribution. Therefore, the electrical conductivity distribution is included in the computation of the elements of the kernel. This point will be further explained below in section 2.2.2. If the electrical conductivity distribution is unknown, time-lapse self-potential data may be inverted with a single snapshot of resistivity, using a homogeneous resistivity distribution, or using a resistivity

distribution inferred from auxiliary data (see for instance Trujillo-Barreto et al., 2004, in electroencephalography, and Revil et al., 2015, in self-potential tomography).

2.2. Inversion modeling

The inversion codes used for both resistivity and self-potential surveys were developed in house using Matlab and Comsol Multiphysics using application programming interface (API) functions. Comsol Multiphysics is used to solve the forward model and the computation of the kernel. The inversion codes calculate sensitivity and update electrical conductivity and source current density vectors during each iteration.

2.2.1. Inversion of resistance data

In the realm of deterministic inversion with Tikhonov regularization, ERT tomography is performed by minimizing the following objective function:

$$\mathrm{P}^{\lambda}(\mathbf{m}) = \left\|\mathbf{W}_d\left(\mathbf{d}(\mathbf{m}) - \mathbf{d}_{obs}\right)\right\|^2 + \lambda\left\|\mathbf{W}_m\left(\mathbf{m} - \mathbf{m}_{ref}\right)\right\|^2. \quad (6)$$

In Equation (6), the matrix $\mathbf{W}_\mathrm{d}$ is related to the data covariance matrix. The data standard deviation is used in populating the diagonal matrix $\mathbf{W}_\mathrm{d}$. The vector $\mathbf{d}(\mathbf{m})$ denotes the predicted data (resistances or apparent resistivity) calculated by solving the Poisson equation using the resistivity model $\mathbf{m}$. The model vector $\mathbf{m}$ denotes here the collection of unknown electrical resistivity for all the cells used to discretize the volume of the tank. We use the log of conductivity as unknowns in $\mathbf{m}$ to ensure positiveness of the conductivity value at each cell. The vector $\mathbf{d}_{\mathrm{obs}}$ denotes the measured resistance or apparent resistivity from the resistivity survey. The parameter λ denotes the regularization parameter, which is optimized using the L-curve approach (see Hansen, 2001 for a general treatment of this problem and Jardani et al., 2008 for

some examples pertaining to self-potential tomography). The matrix $\mathbf{W}_m$ is the weighting matrix, which is related to the model covariance matrix. In our case, a first or second order differential operator can be used. Finally, $\mathbf{m}_{ref}$ denotes a reference model.

During inversion, the electrical conductivity model **m** is updated using the Gauss-Newton method,

$$\mathbf{m}_{i+1} - \mathbf{m}_i \equiv \delta\mathbf{m}, \tag{7}$$

$$\delta\mathbf{m} = -\left[\mathbf{J}^T(\mathbf{W}_d^T\mathbf{W}_d)\mathbf{J} + \lambda\mathbf{W}_m^T\mathbf{W}_m\right]^{-1}[\mathbf{J}^T(\mathbf{W}_d^T\mathbf{W}_d)(\mathbf{d}(\mathbf{m}_i) - \mathbf{d}_{obs}) + \lambda\mathbf{W}_m^T\mathbf{W}_m(\mathbf{m}_i - \mathbf{m}_{ref})], \tag{8}$$

where **J** is the Jacobian matrix and is computed using the principle of reciprocity (Friedel, 2003). At each iteration, the updated parameter vector at iteration i+1 is sent back to Comsol Mutiphysics via an interpolation function. When the change of the objection function (see equation 6) is less than 0.01 or when the value of the objection function is less than 0.01, we consider that the algorithm has converged, and we stop the inversion.

The Active Time Constraint (ATC) time lapse inversion algorithm proposed by Kim et al. (2009) was also attempted in this study. However, the difference between ATC and inverting the data separately was found to be negligible for the tank experiment described below. The benefit of the ATC method is to remove unrelated noise and artifacts from the inversion. The fact that this difference was negligible indicates that good resistance data were obtained during the ERT survey. Therefore, all the data were inverted separately in this paper.

2.2.2. Inversion of self-potential data

From Eq. (5), the voltage response ψ is linearly related to the source current density $\mathbf{J}_s$. Eq. (5) can be written in an integral form as

$$\psi(P) = \int_{\Omega} \mathbf{K}(P, M)\mathbf{J}_s(M)d\Omega, \tag{9}$$

where $\mathbf{K}(P, M)$ is a linear mapping function called the kernel (Trujillo-Barreto et al., 2004), M is the location of the source current density, and P is the self-potential measurement location. Ω is the volume for each current source in the domain, and $d\Omega$ denotes a volume element around the source point M. The kernel is a collection of Green function, which can be determined analytically only for some simplistic geometries (half-space, layered Earth, and so on). The kernel is more often calculated with a numerical method because of its ability to handle boundaries and heterogeneous conductivity distributions. In a 2D problem, the kernel has the form $\mathbf{K} = (\mathbf{K}_x, \mathbf{K}_z)$ and therefore includes two matrices for the horizontal and vertical components of the source current density, respectively. For a 3D problem, the form of the kernel is $\mathbf{K} = (\mathbf{K}_x, \mathbf{K}_y, \mathbf{K}_z)$, and it has components in all three directions. After establishing the kernel, the objective function can be defined as

$$P_{SP}^{\lambda}(\mathbf{m}) = \left\|\mathbf{W}_d(\mathbf{Km} - \mathbf{d}_{obs})\right\|^2 + \lambda\left\|\mathbf{W}_m(\mathbf{m} - \mathbf{m}_{ref})\right\|^2, \tag{10}$$

where $\mathbf{m}$ is the source current density vector, $\mathbf{d}_{obs}$ is the vector of observed self-potential measurement at each self-potential station, $\mathbf{m}_{\text{ref}}$ is the prior reference model vector, and the product $\mathbf{Km}$ denotes the vector of predicted data. The matrix $\mathbf{W}_{\text{m}}$ is a regularization matrix to ensure a stable result. It could have the same form as the one used for the ERT inversion. However, we can also use an identity matrix $\mathbf{I}$ or zeroth order derivative (minimum norm).

From the objective function defined in Eq. (10), the model vector is obtained in a single iteration as (e.g., Jardani et al., 2008)

$$\mathbf{m} = \left[\mathbf{K}^T(\mathbf{W}_d^{\mathbf{T}}\mathbf{W}_d)\mathbf{K} + \lambda(\mathbf{W}_m^T\mathbf{W}_m)\right]^{-1} \cdot \left[\mathbf{K}^T(\mathbf{W}_d^T\mathbf{W}_d)\mathbf{V}_{obs} + \lambda(\mathbf{W}_m^T\mathbf{W}_m)\mathbf{m}_{ref}\right]. \tag{11}$$

As known for the potential-field problems, the inverted results will be localized on the surface of the domain (close to the measurement stations) if only surface measurements are used (Jardani et al., 2008). Depth weighting of the kernel is therefore needed to find a solution that is not weighted close to the top surface of the tank. A diagonal weighting matrix is defined based on the kernel matrix:

$$\mathbf{\Lambda} = \mathrm{diag}(\sum_{i=1}^{N} K_{ij}^2)^{1/4}, \tag{12}$$

where "diag" means creating a diagonal matrix, and N is the number observation data. The rationale behind this weighting matrix is that $\mathbf{\Lambda}^2$ follows the decay of the kernel matrix.

A classical least-square inversion of the self-potential data will lead to a very smooth distribution of the self-potential sources. However, in our case, the source current density is expected to occur only in the area covered by the plume location. Therefore, the source current density is expected to be compact and we need to compact the source current density distribution beyond what is obtained in the classical least square solution with smoothing. We use the *MS* (minimum support) method introduced by Last and Kubik (1983). The *MS*-function is defined as

$$MS = \sum_{k=1}^{M} \frac{m_k^2}{m_{k(i-1)}^2 + \beta^2}, \tag{13}$$

where $m_{k(i-1)}$ is the source current density at iteration i-1, while β is a small threshold number in the *MS* method. With the *MS* function, a new diagonal weighting matrix is established:

$$\mathbf{\Omega} = \mathrm{diag}\left[\sqrt{\frac{\Lambda_{kk}^2}{m_{k-1}^2 + \beta^2}}\right], \tag{14}$$

in which $\mathbf{\Omega}$ is the newly updated weighting matrix. The kernel matrix is revised as $\mathbf{K}^* = \mathbf{K}\Omega^{-1}$, and Eq. (11) is therefore revised to have a new form:

$$\mathbf{m}^* = \left[\mathbf{K}^{*T}(\mathbf{W}_d^{\mathbf{T}}\mathbf{W}_d)\mathbf{K}^* + \lambda(\mathbf{W}_m^T\mathbf{W}_m)\right]^{-1} \cdot \left[\mathbf{K}^{*T}(\mathbf{W}_d^T\mathbf{W}_d)\mathbf{V}_{obs} + \lambda(\mathbf{W}_m^T\mathbf{W}_m)\mathbf{m}_{ref}\right]. \quad (15)$$

The retrieved source current density must be transformed back after each iteration to get an unscaled current density according to $\mathbf{m}=\mathbf{\Omega}^{-1}\mathbf{m}^*$. Normally, the compaction process is done iteratively until the difference between two consecutive iterations is smaller than a prescribed value. However, during the compaction process we must also have a physical understanding of the problems. Otherwise, it could lead to an overly compact source even though the objective function continues to decrease. For example, based on the measured self-potential magnitude, we could roughly know the order of the magnitude for the source current density. For the field test conducted in this paper, the magnitude could not be bigger than 1 A m^{-2}.

3. A sandbox experiment

ERT using miniature electrode arrays is well-suited to the monitoring of contaminant migration and bioremediation in small-scale laboratory experiments (Sentenac et al., 2010; 2015). The movement of a permanganate plume in a TCE-contaminated environment was monitored in an acrylic sandbox using two geophysical methods: Direct Current (DC) resistivity and self-potential (SP). In this section, we describe first the experimental setup and then the approach used to acquire the experimental data during the course of the experiment.

3.1. Rationale for the experiment

Many engineering techniques have been proposed to remediate widespread aquifer contamination (Hyman and Dupont, 2001). In situ chemical oxidation (ISCO) using permanganate ion (MnO_4^-) is one common method used to break down petroleum and other organic compounds in soil and groundwater (Schnarr et al., 1998; Thomson et al., 2007) to

improve water quality. One of the challenges for any remediation method is the effective monitoring of the process. Traditional methods typically rely on geochemical analysis of samples collected from a sparse network of drilled wells, but the limited sampling locations and the influence of aquifer heterogeneity may prevent accurate evaluation and tracking of the remediation program. We hypothesized that the injected ISCO solution will change the local electrical conductivity of the material and generate a concentration gradient, which can be tracked using electrical resistivity tomography and self-potential

3.2. Chemical reaction

The redox reaction between TCE and permanganate can be approximated using Eq. (16) (Yan and Schwartz, 2000):

$$C_2HCl_3(TCE)+2MnO_4^- \rightarrow 2MnO_{2(s)}+2CO_{2(g)}+3Cl^-+H^+ . \quad (16)$$

As a result of this reaction, permanganate ion (MnO_4^-) is removed, and Cl^- and H^+ ions are produced. H^+ is then subsequently removed through protonation of silica surface groups (Hort et al., 2014) and through reaction with bicarbonate present in the pore fluid. These reactions result in a slight increase in the electrical conductivity of the permanganate solution over the unreacted background permanganate conductivity (Hort et al. 2015). However, because of the high concentration of permanganate that was injected compared to the concentration of TCE within the artificial groundwater (50 mM : 1.6 mM) and the relatively small extent of hydrodynamic dispersion that was observed, the fluid conductivity within much of the permanganate plume could likely be approximated based on the original conductivity of the injected solution. In fact, high concentrations of permanganate (35 – 47 mM) were recovered from sampling ports downstream of the collection site 2 hours and 3 hours after injection. While a trail of solid-phase

manganese dioxide (MnO_2) was observed to be left behind as the plume moved, the effects of this precipitate on electrical conductivity are negligible at this concentration of TCE (Hort et al. 2014, 2015). No visible bubbling of CO_2 gas was observed. In this experiment, changes in observed electrical conductivity over time can be assumed to be caused predominantly by the movement of the permanganate plume, which has a significantly higher conductivity than the background artificial groundwater.

3.3. Sandbox setup

The sandbox used in this study had an outer dimension of 0.56 m × 0.076 m × 0.20 m. A total of 32 stainless steel electrodes were installed inside the tank for electrical resistance measurements in four linear arrays (two horizontal with 12 electrodes and two vertical with 6 electrodes, shown in Fig. 1), attached to a plastic housing that was affixed to one wall of the tank. The distance between two consecutive electrodes was 0.03 m. 18-8 stainless steel screws with a 1.9×10^{-3}-m diameter were used as the electrodes. Only a small part of each screw was left to have contact with the porous media, and the rest of it was wrapped with non-conductive epoxy. Each electrode was treated as a point source in the numerical simulation. Two permeable plates were inserted inside the tank to create two reservoir compartments (Figure 1). A woven nylon mesh with 150 μm diameter openings was attached to each plate to avoid sand particles flowing into the reservoirs. 6.3 mL min^{-1} water was circulated between these two reservoirs with an Ismatec IPC peristaltic pump, which created a hydraulic gradient of 0.035 m m^{-1}.

The sandbox was wet-packed by first adding artificial groundwater (4 mM Na^+, 0.2 mM Ca^{2+}, 0.1 mM Mg^{2+}, 2.4 mM Cl^-, 2 mM HCO_3^-, and 0.1 mM SO_4^{2-} in deionized water) amended with dissolved TCE to simulate a contaminated groundwater plume and then adding prepared

sand. The artificial groundwater had a conductivity of 0.048 S m^{-1} at ambient temperature (around 22°C) and a TCE concentration of 1.6 mM just prior to starting the resistivity surveys. The sand was periodically tapped down with a glass rod during filling to remove air bubbles. Unimin #70 industrial quartz sand was chosen for the experiment to be consistent with the experiments performed previously by Hort et al. (2014). The sand was sieved twice with a Tyler #80 sieve, muffled at 550^{o}C to remove organic content, and rinsed with deionized water until the sand was clear and had a conductivity less than 3 μS cm^{-1}. As prepared, the sand had negligible surface conductivity and an intrinsic formation factor (*F*) of about 4 (Hort et al., 2014). Because surface conductivity was negligible, the bulk conductivity of the saturated sand was about 0.012 S m^{-1}. While filling the tank with sand, a small injection tube (x = 0.17 m, y = 0.03 m, bottom of tube 0.067 m below the sand surface) was placed near the upstream reservoir, and two small sampling tubes were placed downstream. After filling, the top of the tank was sealed with Parafilm and plastic wrap to reduce TCE volatilization. The whole tank was maintained under a fume hood for safety reasons. After allowing the fluid to circulate through the tank for 3 hours, 50 mL of artificial groundwater amended with 50 mM $KMnO_4$ (conductivity of 0.604 S m^{-1}) was injected into the pore fluid through the injection tube to simulate the plume.

3.4. Acquisition of geophysical data

The plume moved with the constant hydraulic head gradient from upstream reservoir to the downstream reservoir (right to left in Figure 1). The protocol for the ERT survey was designed to capture the movement of the plume. Sixteen acquisitions (snapshots) were collected with the current injection electrode in the upper horizontal array and retrieving electrode in the bottom array, e.g., 12 and 24 or 11 and 23. Four additional tests were collected between the

vertical arrays. Electrical potential was measured using the skip-one method (Slater et al., 2000). For example, for the current pair 12 and 24, the potentials were measured at electrode pairs 11 and 9, 10 and 8, 9 and 7, etc. A total of 384 potential measurements were taken during each resistivity snapshot.

Resistivity surveys were performed prior to permanganate injection and every half hour beginning immediately after injection (7 surveys were conducted in 3 hours during the experiment). An ABEM-LS multichannel resistivity meter was employed for data acquisition. The protocol was optimized using 4 channels, and with only 2 stacks for each of the 384 measurements to estimate the standard deviation of the measurements. We did not collect reciprocal measurements because of time constraints, though reciprocal datasets could be utilized to check data quality (Kemna et al., 2002; Orozco et al., 2012). A minimum acquisition time of 0.1 s and minimum acquisition delay of 0.1 s were chosen to minimize the total acquisition time in order to capture the plume movement accurately, which corresponds to a 0.2-s current injection period. A duration of 5 minutes was needed to perform the 384 resistivity measurements for each survey. Initial testing of survey time periods showed that these time periods yielded adequately similar results to longer survey times. The acquired data had relatively good quality with 99% of the data having a standard deviation smaller than 1%. Data with errors above this value were removed before the inversion.

Self-potential data were obtained at the surface of the sandbox and taken every hour. A total of 4 surveys were conducted over 3 hours of test duration. Self-potential responses were measured right after each ERT survey at each hour. Ag-AgCl non-polarizing electrodes and a high input impedance voltmeter were used for the measurements. The reference electrode is defined as the electrode connected to the COM of the voltmeter and to which a zero potential is

assigned. This reference electrode was fixed near the downstream reservoir. Thirteen self-potential measurements were taken during each survey with a distance of 3 cm between each station. The electrode drift was checked after each survey and removed from the raw data as indicated in Figures 2a and 2b. After this step, we subtracted the first measurement from all the data (Figure 2c) to reallocate the first data to zero (reference point). These corrected self-potential data were used as input for the self-potential inversion.

3.5. Inversion of the resistivity data

We numerically simulated the process with the finite element software Comsol Multiphysics. The domain was discretized into 53 × 7 × 18 brick elements in *x*, *y* and *z* directions (a total of 6678 elements). Each brick has sides of 10^{-2} m (1 cm) in length. For the inversion, we did not include the two reservoirs that were kept at a constant electrical conductivity of 0.048 S m^{-1}. Therefore, the model vector includes a total of 39×7×18 = 4914 unknown electrical conductivity values. Also, a lower threshold value of 0.022 S m^{-1} (determined by trial and error to separate the background values from the plumes) was applied to the resistivity tomograms to mask unrealistic conductivity changes associated with inversion artifacts. An example of the effect of this thresholding is shown in Figure 3 and an example of 3D resistivity distribution is shown in Figure 4.

3.6. Inversion of the self-potential data

In this study, because the plume moved along the *y*-direction of the sandbox (as visually confirmed), the self-potential problem is solved in the 2D (*x*-*z*) plane. The 2D mesh was the same as that in *x*-*z* plane in the resistance model, which had 53×18=954 brick elements. Since the

kernel values were defined on the node, by excluding the boundary nodes, there were only 646 nodes for placing the dipole sources. The dimension of the kernel $(\mathbf{K}_x, \mathbf{K}_z)$ is therefore 13×1292 (13 measurements and 646×2=1292 source current density unknowns in both *x* and *z* directions).

During kernel calculation, the heterogeneous electrical conductivity σ needs to be considered. A unit dipole source was placed on each node of the mesh. Self-potential was calculated on the measurement location with respect to the reference location by solving Eq. (5). A unit dipole source was placed on each node of the mesh, excluding the boundary nodes for numerical stability reasons. Like the resistance inversion, the two reservoirs were excluded in this inversion since their conductivity was known.

3.7. Results

Figure 4 shows the inverted electrical conductivity distribution 2 hours after the injection of the plume. The tomograms capture the location of the plume but the magnitude of the resistivity change is smaller further away from the electrodes. In reality, the plume should move relatively symmetrically across the tank. This anomaly is due to 3D artifacts associated with the decrease of the sensitivity away from the current electrodes (Kemna et al., 2002). In the following, we will show only slices of the electrical conductivity distribution taken at y = 0.01 m from the electrodes.

Figure 5a shows the extracted 2D electrical conductivity distributions at four different times. All the tomograms are shown at the fourth iteration. Figure 5b shows pictures of the side of the tank taken at the same times. The plume is visible thanks to the characteristic purple color of the permanganate. The brown trace behind the plume is the reaction product MnO_2. This precipitate does not alter the electrical conductivity of the porous material and is therefore not

visible in the conductivity tomogram, at least at the threshold limit used. The conductivity tomograms agree nicely with the movement of the plume.

The inversion was conducted by considering the conductivity variation created by the plume. Because of the movement of the plume during the self-potential survey, we did not have a precise characterization of the plume distribution while making these measurements. Therefore, resistivity tomograms taken every half hour were interpolated to obtain the resistivity distribution during a self-potential survey. When assigning these values, the conductivity variations below the threshold value were not used, and only the variation of conductivity at the plume was picked.

The self-potential signals shown in Figure 2c were inverted to obtain the source current density distribution. Despite the fact that we inverted the horizontal and vertical current density distributions, the vertical components were much smaller (by a factor 100) than the horizontal components; we discuss only the horizontal components below. The source shows a horizontal dipole only, shown in Figure 6. During inversion of the self-potential data, the small number $\beta=10^{-9}$ was picked to produce a compact source and the diagonal weighting number $\lambda=10^{-11}$ was chosen based on L-curve. During the compaction process, we checked not only the objective function Eq. (10), but also the pattern of the compact source. We made sure the source is not over-compacted with a physically unrealistic bigger source current density. Figure 7 shows the predicted self-potential for all four measurements from the estimated source current density at different periods. The trend is close to the 45 degree line.

Figure 8 shows the evolution of the compaction process for the results at t = 2 hours. In order to show the results at early iteration, a different contour legend from Figure 6 is used. The compaction process for the z component is neglected here because of the smaller magnitude. As

the iteration proceeds, the source is pushed downward from the surface location and becomes more compact. At the same time, the magnitude of the source increases.

In Figure 9, we overlapped the estimated source current density vector with the conductivity tomogram. We believe the SP signals are generated from the concentration gradient at the front of the plume and possibly related to the redox reaction occurring between TCE and permanganate. At these four different time periods, the vectors follow the moving direction of the plume, but do not coincide with the front of the plume exactly. We attribute this imprecision to the limited number of SP measurements on the surface and errors during each measurement from noise and drift of electrodes.

Figure 10 shows that the kinetics of the plume movement was captured well by the electrical resistivity and self-potential tomograms. This is an interesting result in itself because very few self-potential measurements were used to localize the position of the plume over time. Figure 11 shows that the self-potential data (Figure 2) are consistent with horizontal dipoles. This is surprising at first, because we expect the self-potential data to be associated with the concentration gradients in the tank and we should therefore see a vertical component in addition to the horizontal components. The vertical component is rather small compared to the horizontal component. We attribute it to the concentration gradient at the front of the advecting plume.

4. A field investigation

4.1. Rationale for the experiment and site description

Sustainable, low-cost and low-impact remediation technology, such as permeable reactive barriers (PRBs), and monitoring tools, such as geophysical methods, are critical for economical risk management of brownfield sites with complex contamination. Implementation

of remediation technology such as PRBs requires an elaborate approach however because the regulatory level of detail required to monitor PRBs, coupled with costly in-situ and laboratory analyses, can quickly render the technology unsustainable. Here we analyze with our 3-D tomographic models electrical resistivity and self-potential data recorded at a former manufactured gas plant in Portadown, Northern Ireland (Figure 12; Kulessa et al., 2006). Integrated electrical geophysical techniques previously supported model development of biogeochemical processes both outside (Doherty et al., 2010; Revil et al., 2010) and inside (Davis et al., 2010) a biological PRB installed at the ~ 1ha site. Previous SP data analysis was solely qualitative, and is substantiated here using formal inversion to locate the source current density.

The area of particular interest for the resistivity and self-potential surveys consisted of shallow aerobic groundwater perched on top of a 0.5 to 2.5-meter clay layer (Doherty et al., 2010). Sitting on top of the thin clay layer are solid waste materials that include ashy metallic clinker and fused iron. Underlying the clay aquiclude is an anaerobic zone of organic-contaminated groundwater that also has a high ammonium concentration. Although thin, the clay layer prevents mixing of the anaerobic organic-contaminated groundwater and the overlying aerobic groundwater with no organic contaminant.

4.2. Acquisition of geophysical data

Ten resistivity surveys were conducted from dotted lines R1 to R10, with 2 meter separation between every two electrode (Figure 12). An IRIS *Syscal R1plus Switch* 36 image system was used for data collection using a *Wenner* protocol, and each 70-m long survey line contained 36 stainless steel electrodes (LaBrecque and Daily, 2008). Inter-line spacing was 5 m,

and 195 measurements were collected for each line. Surface self-potential measurements were collected with lead-lead chloride electrodes (Petiau, 2000) and a high impedance METRA HIT 22S multimeter. At each measurement station, a spade-deep hole was dug and filled with bentonite to ensure good electrode contact with the ground. Self-potential surveys followed the resistivity survey lines, although three additional self-potential survey lines were used (dashed lines in Figure 12). The self-potential electrodes were placed every 5 meters along each line, resulting in a total of 15 measurements per line. The self-potential reference station was located in the non-contaminated part of the field (the solid cross in Figure 12).

4.3. Numerical model setup

4.3.1. Resistivity model

Apparent resistivity data from 10 survey lines were inverted simultaneously in 3D. The forward model domain size was chosen to be 212 m × 202 m × 50 m, and the inverse domain was only located in the center of the forward domain, 70 m × 75 m × 15.92 m. For inverting resistivity, 35 × 30 × 10 = 10,500 cells were used. Each cell is 2 m × 2.5 m in the *x* and *y* directions. In the *z* direction of the inverse domain, incremental size elements were chosen with depth, from 1 m to 2.35 m with an increment ratio of 1.1 (Loke and Barker, 1996). Outside the inverse domain, triangular prism elements were used for the mesh. A uniform resistivity of 20 Ω.m was assigned to the domain to start the inversion based on the site data.

There were 195 apparent resistivity measurements per survey line. Measurements were processed with the Prosys II software from IRIS, and some of the abnormal data were also manually removed before inversion based on visual examination of the apparent resistivity map. In the end, 1303 apparent resistivity measurements were used for inversion.

4.3.2 Self-potential model

When calculating the kernel for inverting SP data, the forward domain was the same as it was in the resistivity model. Also, the domain of the kernel was the same as the inverse domain used in the resistivity inversion, except the meshing was different because SP electrodes were 5 m apart rather than 2 m as they were for resistivity measurements. When choosing the kernel points, only the points covered by the 13 SP survey lines were selected. No kernel points were on the surface and at the bottom of the domain to avoid the boundary effect. In the end, 15 × 13 × 9 = 1755 points were used when calculating the kernel. For the 3D model, the kernel had three components, $\mathbf{K} = (\mathbf{K}_x, \mathbf{K}_y, \mathbf{K}_z)$, with dimensions of 195 × 5625.

The streaming potential component of the SP data was removed using the methodology proposed by Naudet et al. (2003, 2004) and adopted previously by Doherty et al. (2010), and the resultant SP signals only reflect electrochemical and biological sources. All 13 × 15=195 measurements were used to identify the source current density.

4.4. Results

Each individual resistivity survey line was previously analyzed separately by Doherty et al. (2010) using a 2.5-dimensional method (Dey and Morrison, 1979) with Res2Dinv software (Loke and Barker, 1996). The resultant 10 profiles were then interpolated by inverse distance method to obtain a three-dimensional resistivity distribution. Revil et al. (2010) used these results to analyze the cause of the SP anomaly. In this study, all 10 survey lines were inverted together with a 3D model.

The inverted resistivity distribution is shown in Figure 13. In general, the bottom part of the domain is more resistive than the surface area except for the upper left corner. Compared to the inversion of line R2 by Revil et al. (2010), the current results are similar but smoother at the same location. The low resistivity zone is still located around x = 14 m, and only extends from y=15 m to 30 m in the shallow subsurface. The magnitude of this low resistivity is around 5 Ω m. The deeper resistive anomaly is at x = 40 m and extends all across the y direction. It has a maximum value of 40 Ω m. The transition zone between the resistive and less resistive zones is not as sharp as characterized by individually inverting line R2 in Revil et al. (2010). It spreads across a large distance from x = 18 m to 30 m. As shown by Doherty (2002), the conductive zone corresponds to the zone of perched aerobic groundwater containing metallic waste materials above the thin clay layer, while the resistive zone is located where the anaerobic free-phase organic waste plume exists.

The estimated resistivity results were used as input values for calculating the kernel. With the measured SP data on the surface, we could locate a relative compact dipole source around x = 15 and y = 20 m as shown by Figure 14. The largest magnitude is around 0.5 A m^{-2}. We only proceeded with the compaction algorithm described in Section 2.2.2 for 2 iterations. Further compaction would lead to a more compact source, but the magnitude could reach as large as 10 A m^{-2}, which is physically unrealistic.

The source predominantly points in the negative x direction as indicated by the white triangles. The source current density is located close to the surface, and magnitude decreases with depth. The predicted SP data from this estimated source current density matches very well with the measured values as demonstrated in Figure 15. Figure 16 shows the source current density field superimposed on the estimated resistivity field. The source current density field is

observed near the conductive part of the tomogram, to the left of the transition zone. Because the influence of streaming potential was already removed before identifying the source current density, the estimated results mainly reflect electrochemical and biological sources.

At this site, the measured surface self-potential anomaly ranges from -455 mV to +380 mV, which means a very large peak to peak anomaly of 800 mV, and the estimated source current density is about 0.5 A m^{-2}. During the compaction process, the source current density is increased because of a required compact source. However, similar to the tank experiment results in section 3.7, the source current density anomaly is due to a concentration gradient. In this field test, the measured redox potential values only range from -161mV to +97mV, and redox reactions could drive such a large dipolar self-potential distribution alone. The large magnitudes of the self-potential gradient and source current density are catalyzed by microbial activity occurring in the anaerobic zone (Doherty et al., 2010; Revil et al., 2010). The activity of the anaerobic microorganisms may produce an abundance of anions, while oxidation of the overlying iron wastes may produce a positively charged environment. The thin clay layer may act as a permeable membrane for the transfer of charges between the two regions (see Revil et al., 2010).

5. Conclusion

In the current study, we have tested the efficiency of using both DC resistivity and self-potential measurements to track or locate a conductive anomaly either for remediation monitoring monitoring or contaminant localization. During the sandbox experiment, the self-potential inversion produced a horizontal dipole source current density that remained at the front of the plume as it moved across the tank. The location of the plume could be verified both

through resistivity measurements and visual observation of the plume. The self-potential source current density is possibly associated with the strong concentration gradient between the permanganate plume and the surrounding artificial groundwater. At the field site, where a thin clay unit separates an overlying perched aerobic groundwater unit containing man-emplaced metal contaminants from underlying anaerobic organic-contaminated groundwater, a compact horizontal dipole source was located close to the conductive (metallic) region. The 0.5 A m^{-2} magnitude source current density is potentially associated with microbially enhanced redox reactions between the aerobic and anaerobic zones.

In both the sand box and field experiments, similar information was obtained using both resistivity and self-potential surveys. However, self-potential may require fewer measurements and less processing time when compared with resistivity surveys. In fact, only 13 surface self-potential data points were needed during the sandbox experiment to locate the front edge of the permanganate plume. This suggests that the self-potential survey may be a promising fast method for the monitoring certain contaminants or methods of remediation.

Acknowledgement. This work is funded by the Office of Science (BER) and Chevron Energy Technology Company (Grant #CW852844). We thank the Associate Editor, Dongmei Han, and the two referees for their useful comments. This is the Boone Pickens School of Geology contribution # 2015-xx.

References

Cassiani, G., V. Bruno, A. Villa, N. Fusi, and A.M. Binley, 2006, A saline trace test monitored via time-lapse surface electrical resistivity tomography: Journal of Applied Geophysics, 59, no. 3, 244–259, doi:10.1016/j.jappgeo.2005.10.

Castermant, J., C.A. Mendonça, A. Revil, F. Trolard, G. Bourrié and N. Linde, 2008, Redox potential distribution inferred from self-potential measurements associated with the corrosion of a burden metallic body: Geophysical Prospecting, 56, no. 2, 269-282.

Comina, C., R. M. Cosentini, G. Della Vecchia, S. Foti, and G. Musso, 2010, Hydro-chemo-mechanical processes in soil samples: monitoring through electrical resistivity tomography, EPJ Web of Conferences, 6, 22012.

Comina, C., R. M. Cosentini, G. Della Vecchia, S. Foti, and G. Musso, 2011, 3D-electrical resistivity tomography monitoring of salt transportin homogeneous and layered soil samples, Acta Geotechnica, 6, 195–203, doi: 10.1007/s11440-011-0146-3.

Daily, W., and A. Ramirez, 1995, Electrical resistance tomography during in-situ trichloroethylene remediation at the Savannah River Site: Journal of Applied Geophysics, 33, no. 4, 239-249.

Davis, C. A., L. D. Slater, B. Kulessa, A. S. Ferguson, E. A. Atekwana, R. Doherty, and R. Kalin, 2010, Self-potential (SP) signatures associated with an injection experiment at an in-situ biological permeable reactive barrier (PRB): Near Surface Geophysics, 8, no. 6, 541-551, doi: 10.3997/1873-0604.2010034.

Dey, A., and H. F. Morrison, 1979, Resistivity modeling for arbitrarily shaped two-dimensional structures: Geophysical Prospecting, 27, no. 1, 106-136.

Doherty, R., 2002, Modelling a permeable reactive barrier (PRB) in a manufactured gas plant site, Portadown, Northern Ireland,:Unpublished PhD thesis, Queen's University Belfast.

Doherty, R., B. Kulessa, A. S. Ferguson, M. J. Larkin, L. A. Kulakov, and R. M. Kalin, 2010, A microbial fuel cell in contaminated ground delineated by electrical self-potential and normalized induced polarization data: Journal of Geophysical Research: Biogeosciences, 115, G3, G00G08.

Friedel, S., 2003, Resolution, stability and efficiency of resistivity tomography estimated from a generalized inverse approach: Geophysical Journal International, 153, no. 2, 305-316, doi: 10.1046/j.1365-246X.2003.01890.x.

Gehman, C.L., D.L. Harry W.E. Sanford J.D. Stednick N.A. Beckman, 2009, Estimating specific yield and storage change in an unconfined aquifer using temporal gravity surveys: Water Resources Research, 45, W00D21, doi: 10.1029/2007WR006096.

Hansen, P.C., 2001, The L-Curve and its use in the numerical treatment of inverse problems, Computational Inverse Problems in Electrocardiology, 119-142; WIT Press.

Hort, R.D., A.. Revil, J. Munakata-Marr, 2014, Analysis of sources of bulk conductivity change in saturated silica sand after unbuffered TCE oxidation by permanganate: Journal of Contaminant Hydrology, no. 165, 11-23, doi: 10.1016/j.jconhyd.2014.07.003.

Hort, R. D., A. Revil, J. Munakata-Marr, *and* D. Mao *(*2015*),* Evaluating the potential for quantitative monitoring of in situ chemical oxidation of aqueous-phase TCE using in-phase and quadrature electrical conductivity, Water Resour. Res., 51, *doi:*10.1002/2014WR016868.

Hyman, M., and R. Dupont, 2001, Groundwater and Soil Remediation: process design and cost estimating of proven technologies: American Society of Civil Engineers Press, Reston, 517 pp.

Hubbard, S.S., J.S. Chen, J. Peterson, E.L. Majer, K.H. Williams, D.J. Swift, B. Mailloux, and Y. Rubin, 2001, Hydrogeological characterization of the South Oyster Bacterial Transport Site using geophysical data: Water Resources Research, no. 37, 2431-2456.

Ikard, S.J., and A. Revil, 2014, Self-potential monitoring of a thermal pulse advecting through a preferential flow path: Journal of Hydrology, no. 519(A), 34-49, doi: 10.1016/j.jhydrol.2014.07.001.

Ikard, S.J., A. Revil, Jardani, W.F. Woodruff, M. Parekh, and M. Mooney, 2012, Saline pulse test monitoring with the self-potential method to non-intrusively determine the velocity of the pore water in leaking areas of earth dams and embankments: Water Resources Research, no. 48, W04201, doi:10.1029/2010WR010247.

Jardani, A., A. Revil, A. Bolève, J.P. Dupont, 2008, Three-dimensional inversion of self-potential data used to constrain the pattern of groundwater flow in geothermal fields: Journal of Geophysical Research, no. 113(B9), B09204, doi:10.1029/2008GL035025.

Jardani, A., A. Revil, and J.P. Dupont, 2013, Stochastic joint inversion of hydrogeophysical data for salt tracer test monitoring and hydraulic conductivity imaging: Advances in Water Resources, no. 52, 62-77, doi: 10.1016/j.advwatres.2012.08.005.

Karaoulis, M., A. Revil, and D. Mao, 2014. Localization of a coal seam fire using combined self-potential and resistivity data: International Journal of Coal Geology, no. 128–129: 109-118, doi: 10.1016/j.coal.2014.04.011.

Karaoulis M., A. Revil, B. Minsley, M. Todesco, J. Zhang, and D.D. Werkema, 2014, Time-lapse gravity inversion with an active time constraint: Geophysical Journal International, no. 196, 748–759, doi:10.1093/gji/ggt408.

Kemna, A., B. Kulessa, and H. Vereecken, 2002, Imaging and characterisation of subsurface solute transport using electrical resistivity tomography (ERT) and equivalent transport models.:Journal of Hydrology, no. 267(3–4), 125-146.

Kim, J.-H., M.-J. Yi, S.-G. Park, and J.G. Kim, 2009. 4-D inversion of DC resistivity monitoring data acquired over a dynamically changing earth model, Journal of Applied Geophysics, 68, no. 4, 522-532.

Kulessa, B., B. Hubbard, and G. Brown, 2003, Cross-coupled flow modelling of coincident streaming and electrochemical potentials, and application to subglacial self-potential (SP) data. Journal of Geophysical Research, 108, no. B8, 2381, doi: 10.1029/2001JB001167.

Kulessa, B., R. Kalin, R. Doherty, and D. Phillips, 2006, Self-potential (SP) and active electrical geophysical assessment of bioremediation at a contaminated gasworks plant, AGU Spring Meeting Abstracts, 1, 04.

LaBrecque, D., and X. Yang, 2001, Difference inversion of ERT Data: a fast inversion method for 3-D in situ monitoring: Journal of Environmental and Engineering Geophysics, 6, no. 2, 83-89.

LaBrecque, D., and W. Daily, 2008, Assessment of measurement errors for galvanic-resistivity electrodes of different composition,: Geophysics, 73, no. 2, F55-F64.

Last, B.J., and K. Kubik, 1983, Compact gravity inversion, Geophysics, 48, no. 6, 713-721.

Leinov, E., J. Vinogradov, and M.D. Jackson, 2010, Salinity dependence of the thermoelectric coupling coefficient in brine-saturated sandstones: Geophysical Research Letters, 37, no. 23, L23308, doi: 10.1029/2010GL045379.

Loke, M. H., and R. D. Barker, 1996, Practical techniques for 3D resistivity surveys and data inversion1: Geophysical Prospecting, 44, no. 3, 499-523.

Loke, M.H., J.E. Chambers, D.F. Rucker, O. Kuras, and P.B. Wilkinson, 2013, Recent developments in the direct-current geoelectrical imaging method: Journal of Applied Geophysics, 95, 135-156, doi:10.1016/j.jappgeo.2013.02.017.

Maineult, A., Y. Bernabé, and P. Ackerer, 2004, Electrical response of flow, diffusion, and advection in a laboratory sand Box. Vadose Zone Journal, 3, no. 4, 1180-1192.

Maineult, A., Y. Bernabé, and P. Ackerer, 2005. Detection of advected concentration and pH fronts from self-potential measurements: Journal of Geophysical Research, 110, no. B11, B11205, doi:10.1029/2005JB003824.

Maineult, A., Y. Bernabé, and P. Ackerer, 2006, Detection of advected, reacting redox fronts from self-potential measurements: Jounal of Contaminant Hydrology, 86, no. 1–2, 32-52.

Martínez-Pagán, P., A. Jardani, A. Revil, and A. Haas, 2010. Self-potential monitoring of a salt plume: Geophysics, 75, no. 4, WA17-WA25, doi: 10.1190/1.3475533.

Naudet, V., A. Revil, J.-Y. Bottero, and P. Bégassat, 2003. Relationship between self-potential (SP) signals and redox conditions in contaminated groundwater: Geophysical Research Letters, 30, no. 21.

Naudet, V., A. Revil, E. Rizzo, J.-Y. Bottero, and P. Bégassat, 2004, Groundwater redox conditions and conductivity in a contaminant plume from geoelectrical investigations: Hydrology and Earth System Sciences Discussions, 8, no. 1, 8-22.

Orozco, A. F., A. Kemna, and E. Zimmermann, 2012, Data error quantification in spectral induced polarization imaging, Geophysics, 77, no.3, E227-E237.

Petiau, G., 2000, Second generation of lead-lead chloride electrodes for geophysical applications,:Pure and Applied Geophysics, 157, no. 3, 357-382.

Power, C., J. I. Gerhard, P. Tsourlos, P. Soupios, K. Simyrdanis, and M.. Karaoulis, 2015, Improved time-lapse electrical resistivity tomography monitoring of dense non-aqueous phase liquids with surface-to-horizontal borehole arrays: Journal of Applied Geophysics, 112, 1-13, doi: 10.1016/j.jappgeo.2014.10.022.

Revil, A., 1999, Ionic diffusivity, electrical conductivity, membrane and thermoelectric potentials in colloids and granular porous media: A unified model: Journal of colloid and interface science, 212, no. 2, 503-522.

Revil, A., D. Hermitte, M. Voltz, R. Moussa, J.-G. Lacas, G. Bourrié, and F. Trolard, 2002, Self-potential signals associated with variations of the hydraulic head during an infiltration experiment: Geophysical Research Letters, 29, no. 7, 1106, doi: 10.1029/2001GL014294.

Revil, A., F. Trolard, G. Bourrié, J. Castermant, A. Jardani, and C.A. Mendonça, 2009, Ionic contribution to the self-potential signals associated with a redox front: Journal of Contaminant Hydrology, 109, no. 1–4, 27-39.

Revil, A., C.A. Mendonça, E.A. Atekwana, B. Kulessa, S.S. Hubbard, and K.J. Bohlen, 2010, Understanding biogeobatteries: Where geophysics meets microbiology: Journal of Geophysical Research: Biogeosciences, 115 no. G1, G00G02.

Revil A., M. Skold, M. Karaoulis, M. Schmutz, S.S. Hubbard, T.L. Mehlhorn, and D.B. Watson 2013, Hydrogeophysical investigations of the former S-3 ponds contaminant plumes, Oak Ridge Integrated Field Research Challenge site, Tennessee: Geophysics, 78, no. 4, EN29-EN41, doi: 10.1190/geo2012-0177.1.

Revil, A., 2013a, Effective conductivity and permittivity of unsaturated porous materials in the frequency range 1 mHz–1GHz: Water Resources Research, 49, 306-327, doi:10.1029/2012WR012700.

Revil, A., 2013b, On charge accumulations in heterogeneous porous materials under the influence of an electrical field: Geophysics, 78, no. 4, D271–D291, doi: 10.1190/GEO2012-0503.1.

Revil A., D. Mao, A. K. Haas, M. Karaoulis, L. Frash, 2015, Passive electrical monitoring and localization of leakages in wells using electrography: Journal of Hydrology, 521, 286-301, doi: 10.1016/j.jhydrol.2014.12.003.

Risgaard-Petersen, N., A. Revil. P. Meister, and L.P. Nielsen, 2012, Sulfur, iron-, and calcium cycling associated with natural electric currents running through marine sediment: Geochimica et Cosmochimica Acta, 92, 1–13.

Rizzo, E., B. Suski, A. Revil, S. Straface, and S. Troisi, 2004, Self-potential signals associated with pumping tests experiments: Journal of Geophysical Research, 109, no. B10, B10203, doi: 10.1029/2004JB003049.

Schnarr, M., C. Farquhar, E. Hood, T. Gonullu, and B. Stickney, 1998, Laboratory and controlled field experiments using potassium permanganate to remediate trichloroethylene and perchloroethylene DNAPLs in porous media: Journal ofContaminant Hydrology, 29, no. 3, 205-224.

Sentenac, P., A. Montinaro and B. Kulessa, 2010, Diesel transport monitoring in simulated unconfined aquifers using miniature resistivity arrays: Environmental Earth Sciences, 61, no. 1, 107-114. doi:10.1007/s12665-009-0325-9.

Sentenac, P., T. Hogson, H. Keenan, and B. Kulessa, 2015, Small scale monitoring of a bioremediation barrier using miniature electrical resistivity tomography: Journal of Applied Geophysics, 115, 24-31, doi:http://dx.doi.org/10.1016/j.jappgeo.2014.11.006.

Singha, K., and S.M. Gorelick, 2005, Saline tracer visualized with three-dimensional electrical resistivity tomography: Field-scale spatial moment analysis: Water Resources Research, 41, W05023. doi:10.1029/2004WR003460.

Slater, L., 2007, Near surface electrical characterization of hydraulic conductivity: From petrophysical properties to aquifer geometries—A review: Survey in Geophysics, 28, no. 2-3, 169-197.

Slater, L., A.M. Binley, W. Daily, and R. Johnson, 2000, Cross-hole electrical imaging of a controlled saline tracer injection: Journal of Applied Geophysics, 44, no. 2–3, 85-102.

Suski, B., E. Rizzo, and A. Revil, 2004, A sandbox experiment of self-potential signals associated with a pumping test: Vadose Zone Journal, 3(4), 1193-1199.

Thomson, N.R., E.D., Hood, and G.J. Farquhar, 2007, Permanganate treatment of an emplaced DNAPL source: Ground Water Monitoring & Remediation, 27, no. 4, 74-85.

Titov, K., A. Revil, P. Konosavsky, S. Straface, and S. Troisi, 2005, Numerical modelling of self-potential signals associated with a pumping test experiment: Geophysical Journal International, 162, no. 2, 641-650.

Trujillo-Barreto, N.J., E. Aubert-Vázquez, and P.A. Valdés-Sosa, 2004, Bayesian model averaging in EEG/MEG imaging: NeuroImage, 21, no. 4, 1300-1319.

Williams, K. H., A. Kemna, M. J. Wilkins, J. Druhan, E. Arntzen, A. L. N'Guessan, P. E. Long, S. S. Hubbard, and J. F. Banfield, 2009, Geophysical Mmonitoring of coupled microbial and geochemical processes during stimulated subsurface bioremediation: Environmental Science and Technology, 43, no. 17, 6717-6723.

Yan, Y.E., and F.W. Schwartz, 2000, Kinetics and mechanisms for TCE oxidation by permanganate, Environmental Science and Technology, 34, no. 12, 2535-2541.

Ye, M., R. Khaleel, and T.-C.J. Yeh, 2005, Stochastic analysis of moisture plume dynamics of a field injection experiment, Water Resources Research, 41, no. 3, 1-13.

Figures

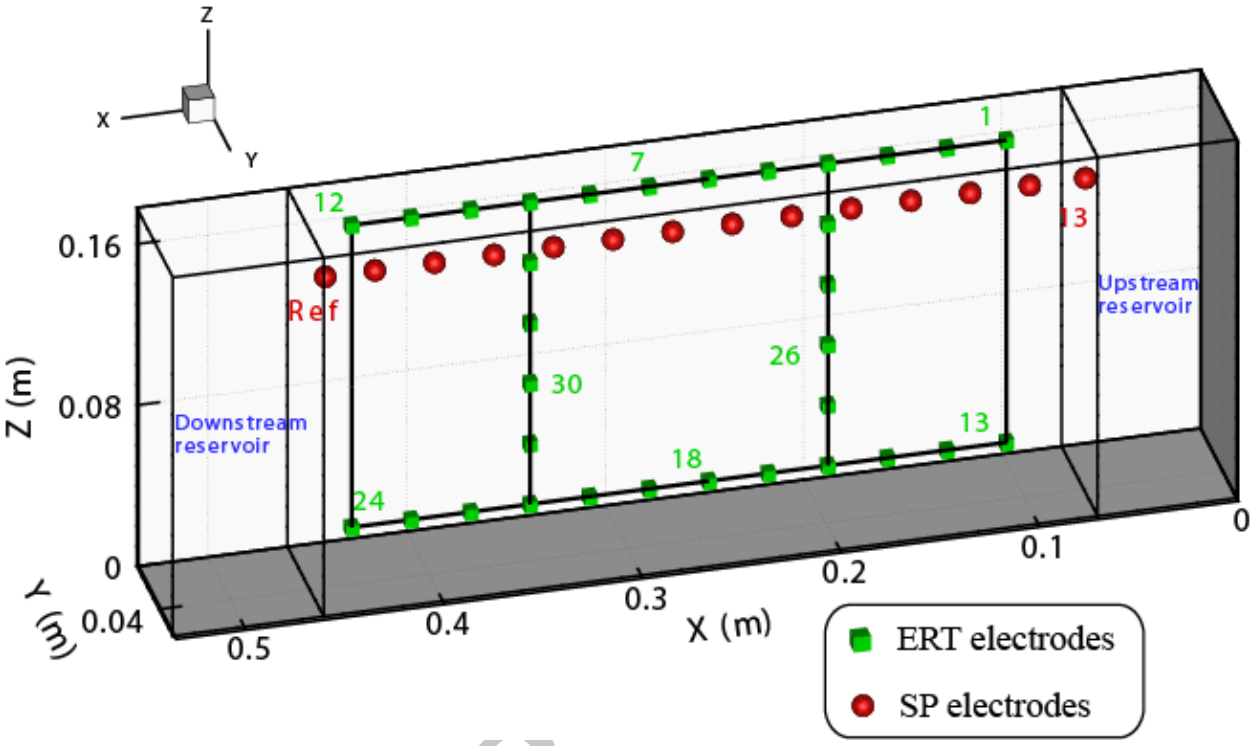

Figure 1. Configuration of the sandbox used in the experiment with the position of the electrodes used for the self-potential (SP) and resistivity (ERT) surveys. Note that the self-potential measurements are performed only from the top surface of the tank. The permanganate plume moves from right to left driven by the hydraulic head gradient between the two reservoirs.

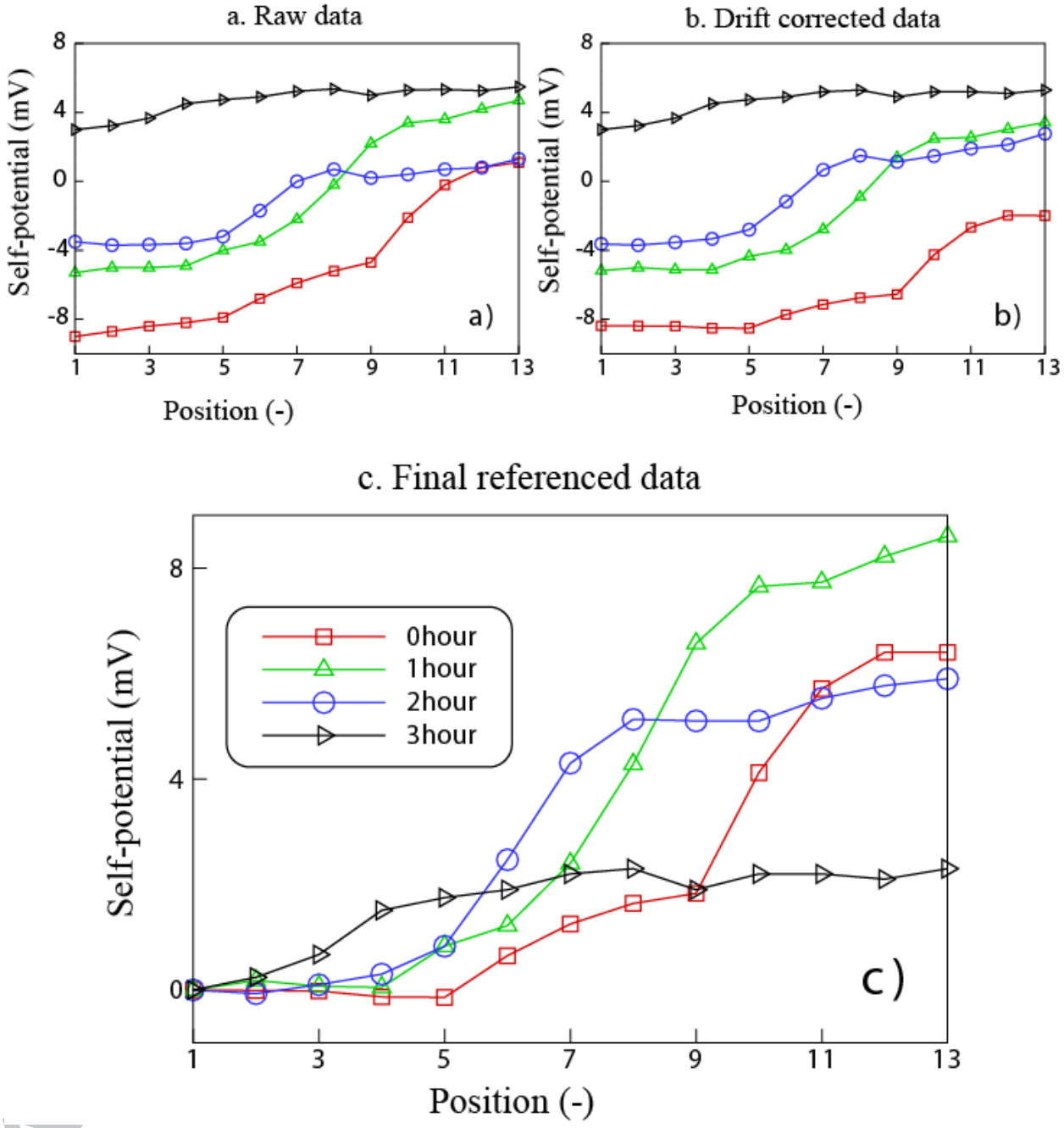

Figure 2. Self-potential profiles. **a.** Raw data. **b.** Drift removed. **c.** Final self-potential profiles used for the inversion. The first electrode is used as a common reference for each profile and over time.

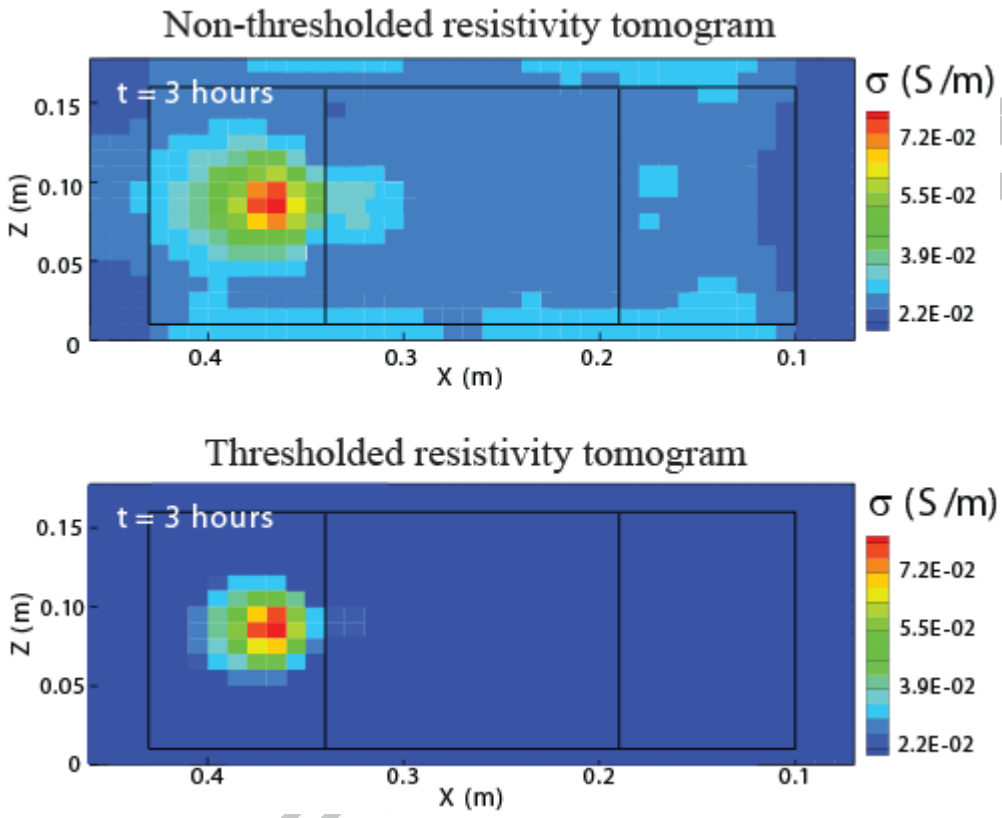

Figure 3. Thresholding the resistivity tomograms (here at t = 3 hours after the injection of the permanganate). The value of the threshold is fixed at 2.2×10^{-2} S m^{-1}.

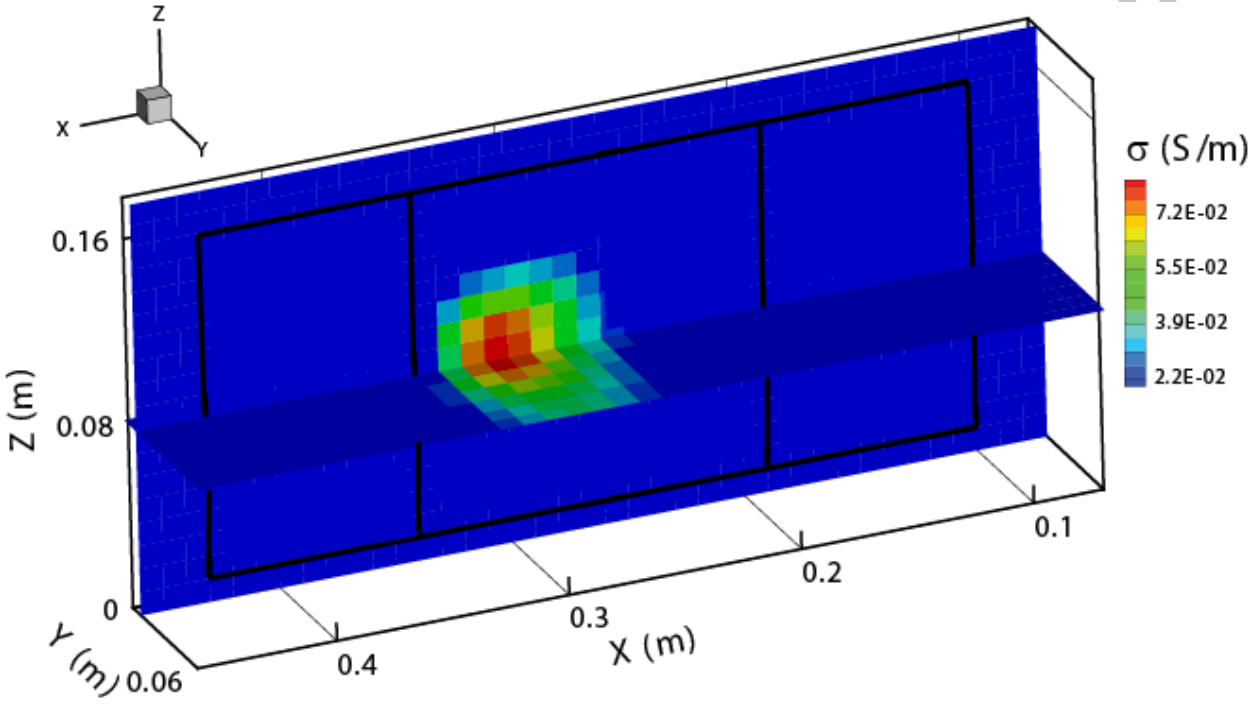

Figure 4. 3D inverted electrical resistivity tomogram at t = 2 hours after the injection of the permanganate. The solid black lines indicate the electrode locations on the side of the sandbox.

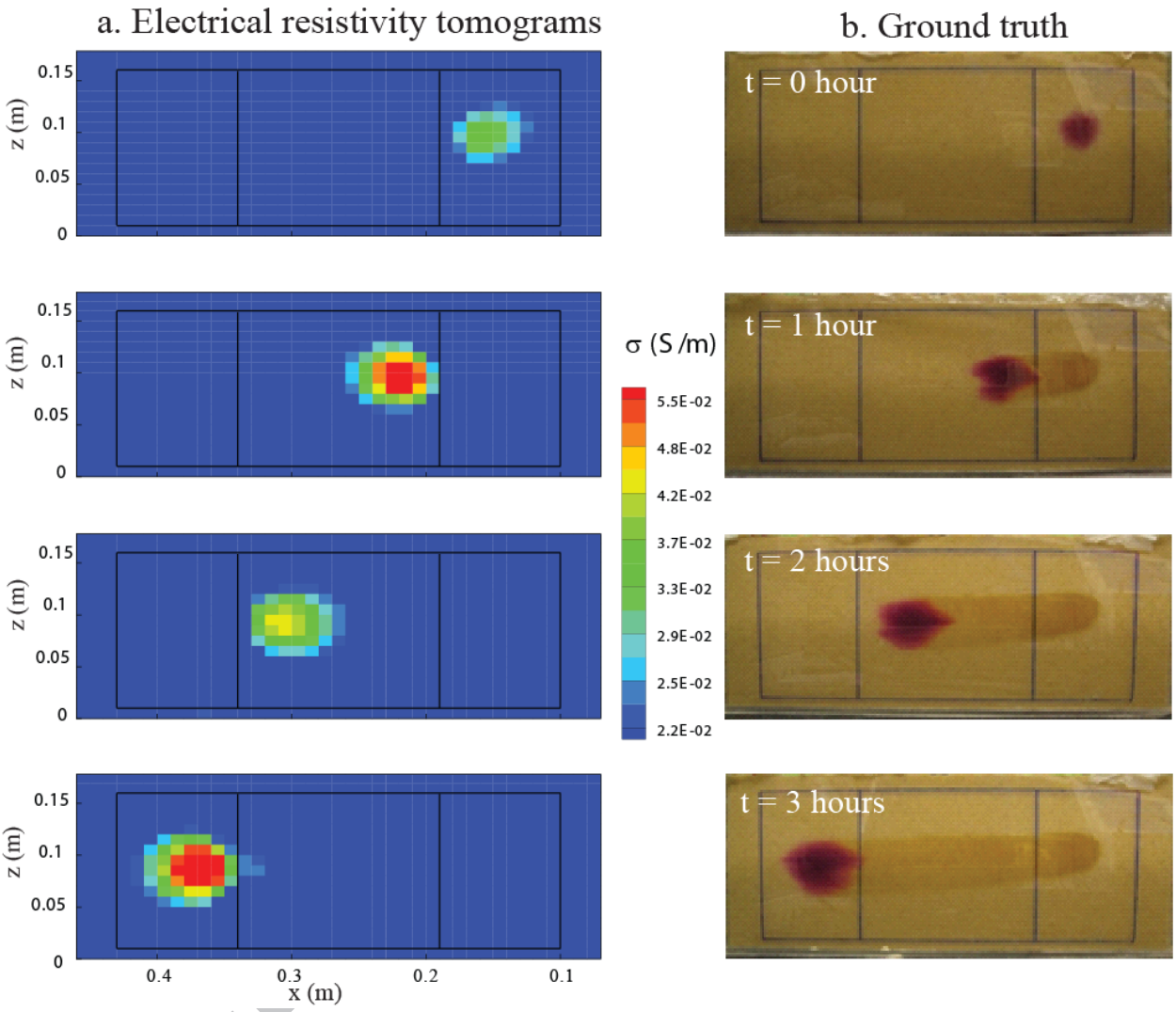

Figure 5. Comparison between the thresholded electrical resistivity tomograms (at the fourth iteration) and a set of photos showing the position of the plume at four different times. **a.** Extracted 2D slice images of the electrical resistivity distributions. **b.** Photos taken during the ERT survey. Note that the shadow left by the migration of the plume corresponds to the solid product MnO_2 associated with the chemical reaction described in the main text. The black plain lines are similar to those shown in Figure 1 showing the position of the electrodes.

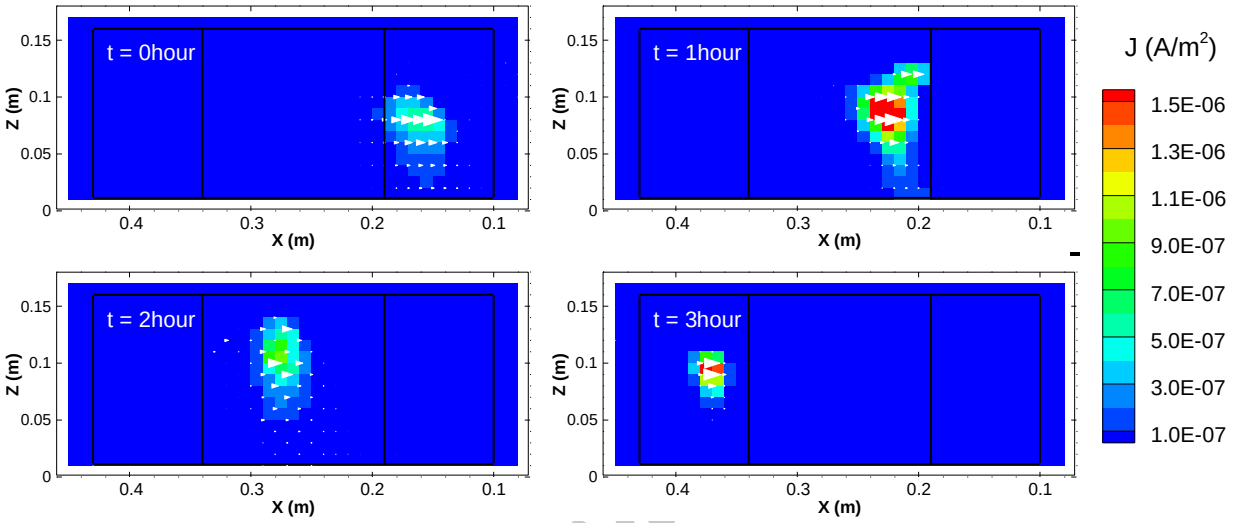

Figure 6. Inverted source current density distributions at four distinct times. The white triangles indicate the directions of the source current density and they mainly point in the negative *x* direction (to the right in this figure).

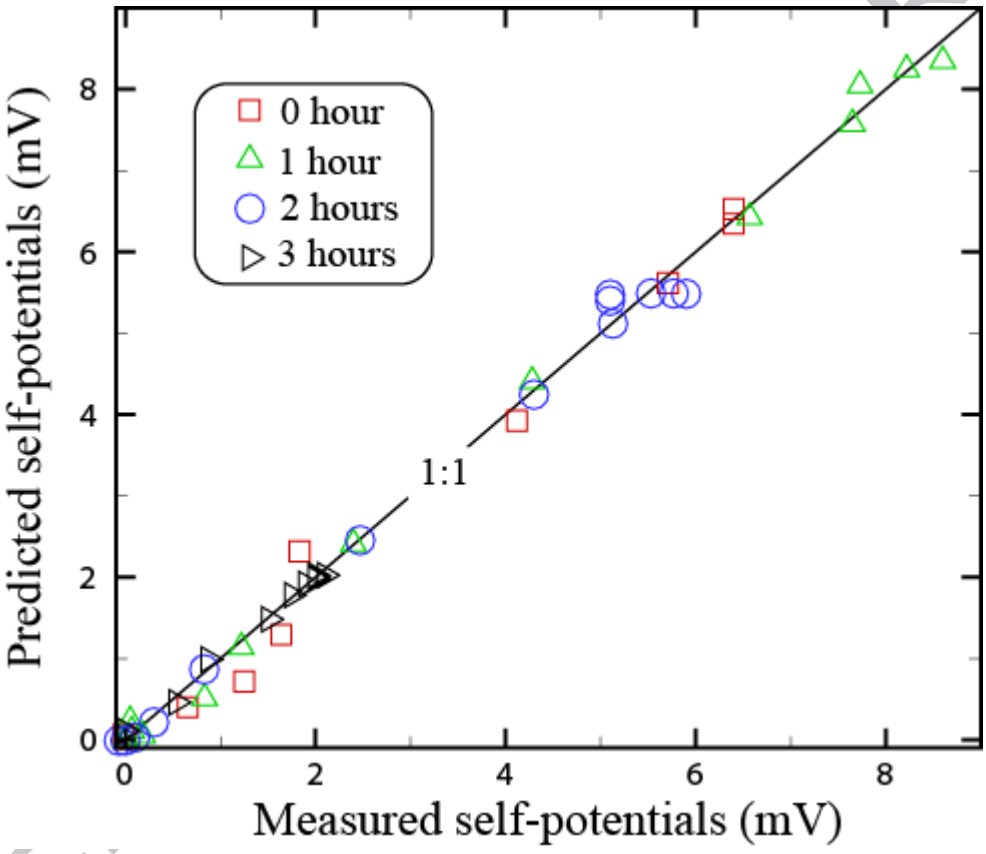

Figure 7. Comparison between measured and predicted self-potential signals for the four different periods. The self-potential data are well-reproduced by the inverted source current density distributions.

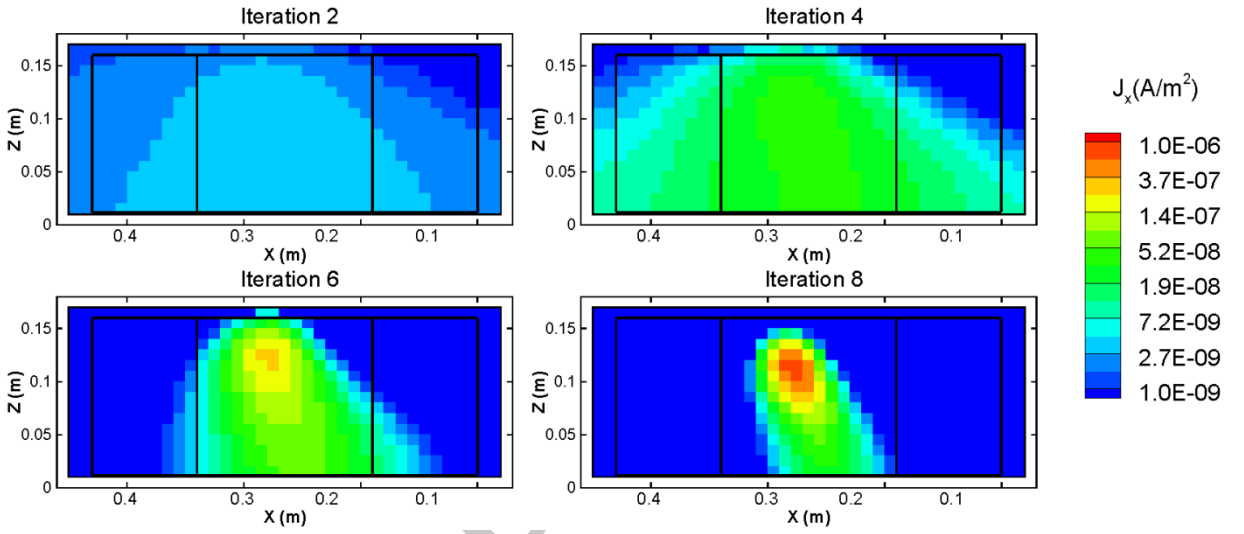

Figure 8. Evolution of the source current density at t = 2 hours at four different iteration numbers during the compaction process of the support of the source (iterations 2, 4, 6, and 8, respectively).

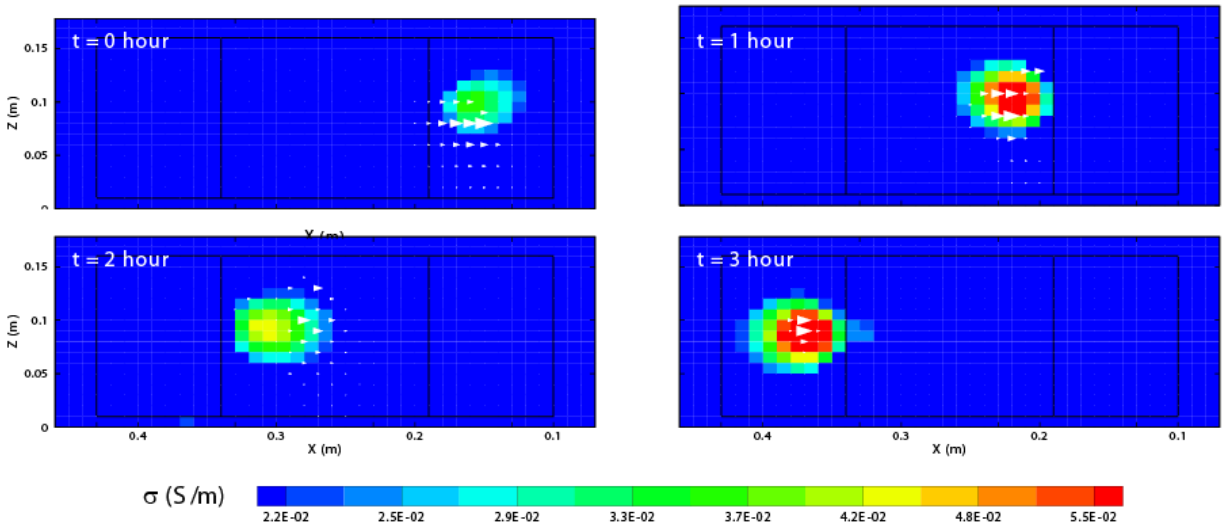

Figure 9. Estimated source current density vectors overlapped with conductivity tomograms at different periods of the plume movement. The flow of the pore water occurs from right to left.

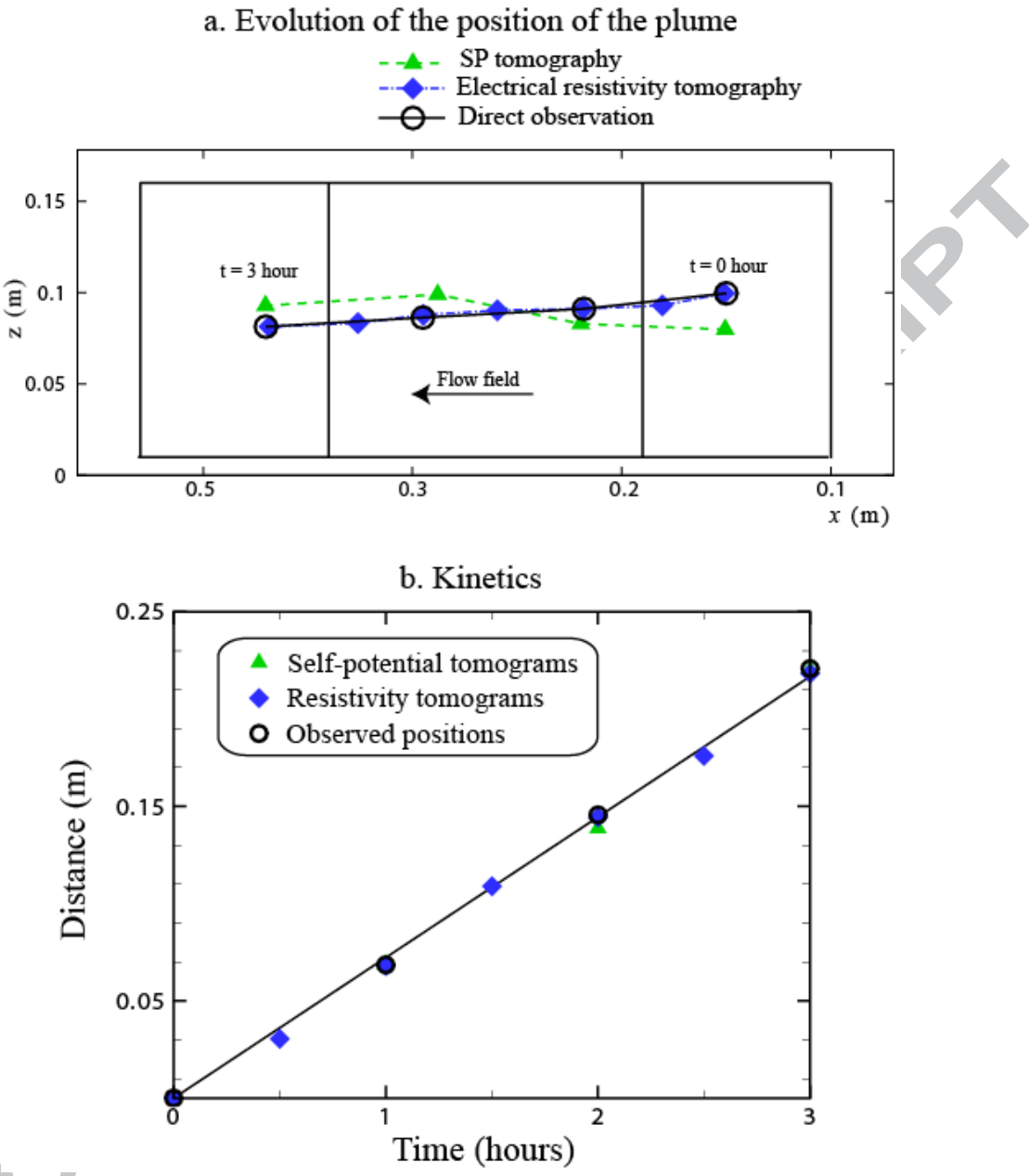

Figure 10. Position of the plumes according to the different methods. **a.** Locations of the centers of the plume over time shown in Figures 5 and 6. The black circles are the center of the plume estimated by visual inspection from the photos taken during the experiment. **b.** The distances of the plume centers from the injection location are plotted with time along the curvilinear distance following the trajectory of the plume (plain line in Figure 10a). All the data from the tomograms and the observations are consistent with a mean velocity of 0.073 m hour^{-1}.

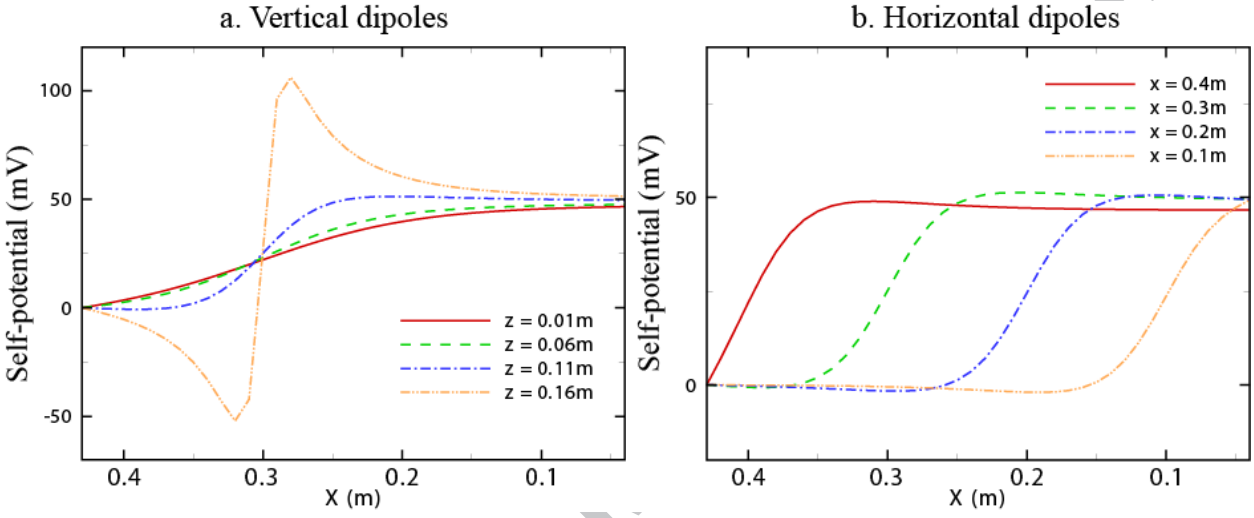

Figure 11. Self-potential signals measured on the surface of the tank. **a.** Self-potential response from current sources at different elevation while at the same horizontal location x = 0.2 m (the z = 0.16 m represents a shallow current source). **b.** Self-potential response from current sources at different horizontal locations while elevation is fixed at z = 0.11 m. x = 0.1 m is close to the upstream reservoir.

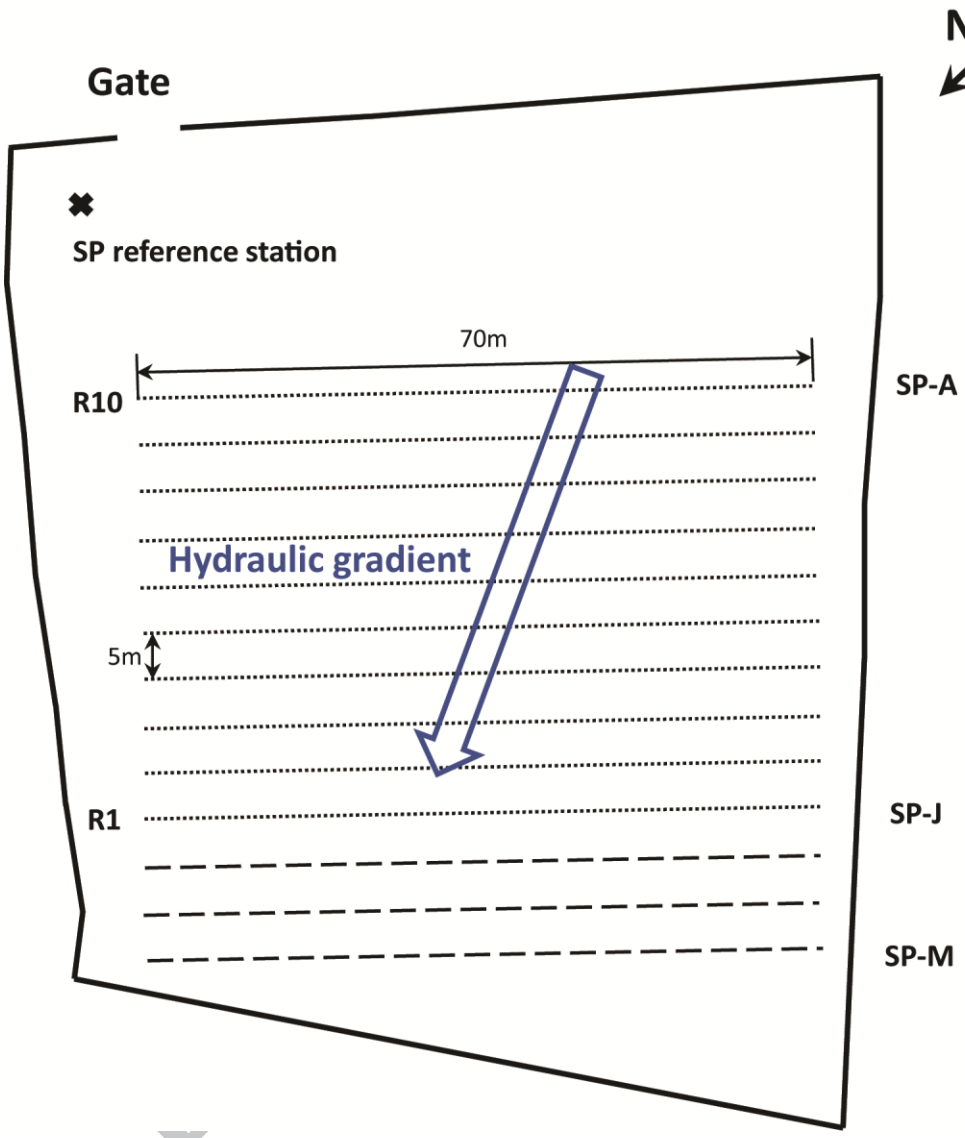

Figure 12. Sketch of the test site (Portadown, Northern Ireland). The solid lines show the limits of the factory property. The ten dashed lines (R1 to R10) indicate the position of the electrical resistivity surveys (2 meter spacing between the electrodes). There is a total of 13 lines for the self-potential survey (the 10 resistivity lines plus 3 lines named SP-A to SP-M with 5 meter separation between each station). The self-potential reference station was chosen in the non-contaminated part of the property indicated by a solid cross. The arrow represents the local hydraulic gradient direction and therefore in principle the flow direction.

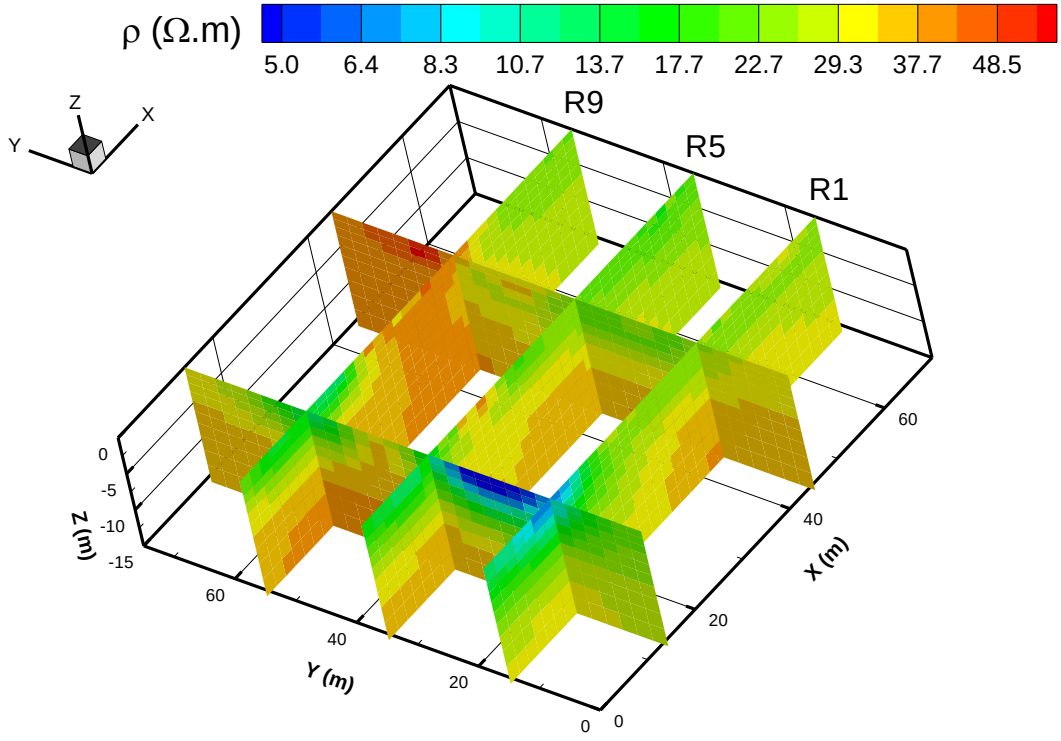

Figure 13. 3D inversion of the electrical resistivity distribution. R1, R5 and R9 denote three of the survey lines. Note the area of low electrical resistivity (below 10 Ohm m). This area corresponds to the area exhibiting a negative self-potential anomaly at the ground surface.

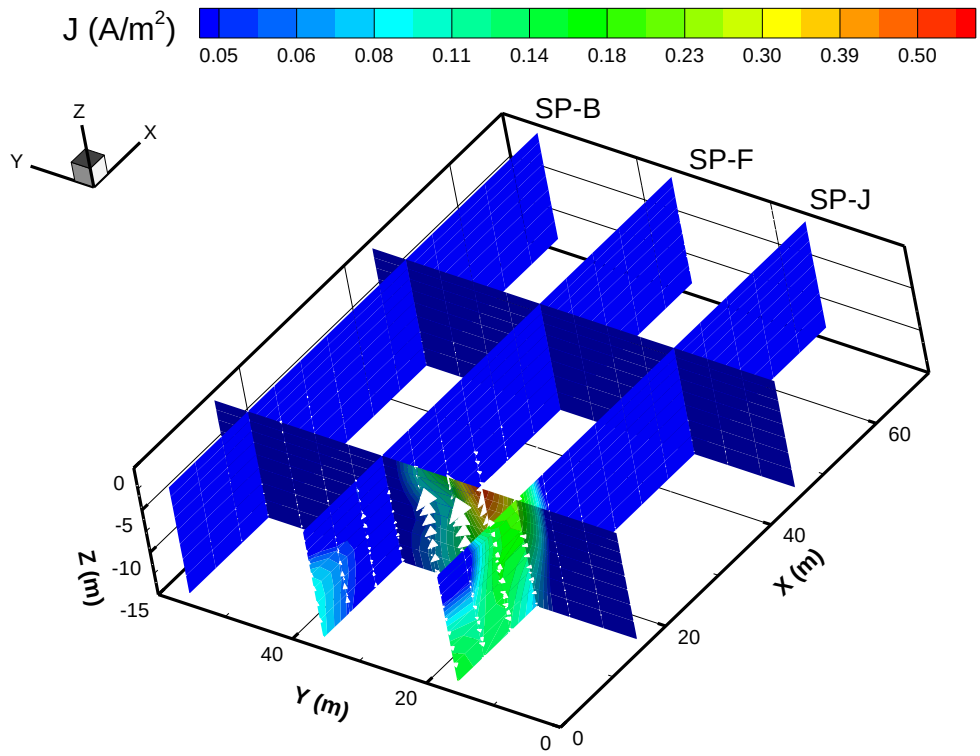

Figure 14. Magnitude of the estimated source current density (in A m^{-2}). The maximum source current density value is approximately 0.5 A m^{-2}. The white triangles indicate the direction of the source current density vectors and mainly points in the negative *x* direction.

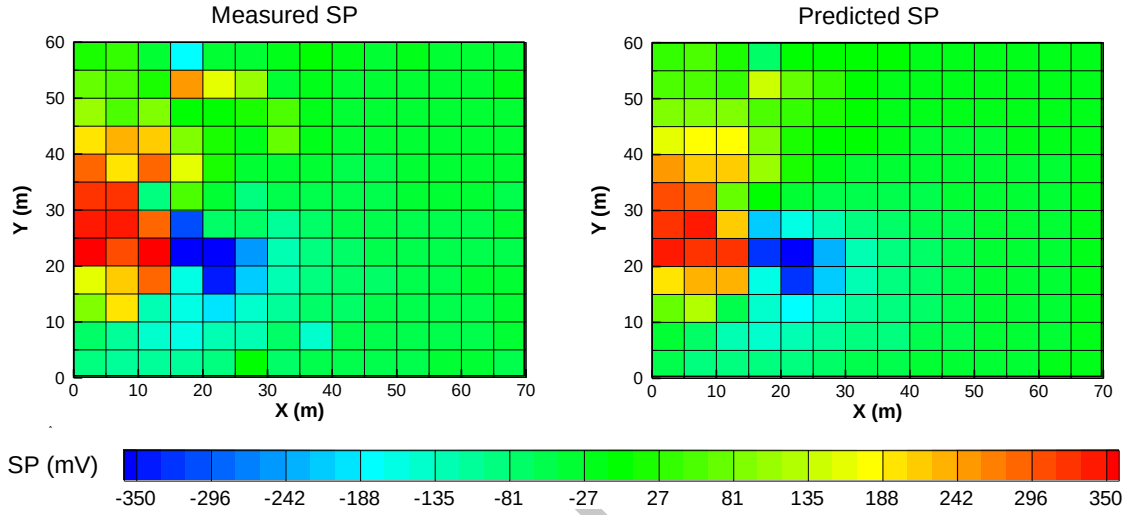

Figure 15. Comparison between the measured and predicted self-potential distributions at the ground surface (expressed in mV). The predicted self-potential map is based on the source current density shown in Figure 14.

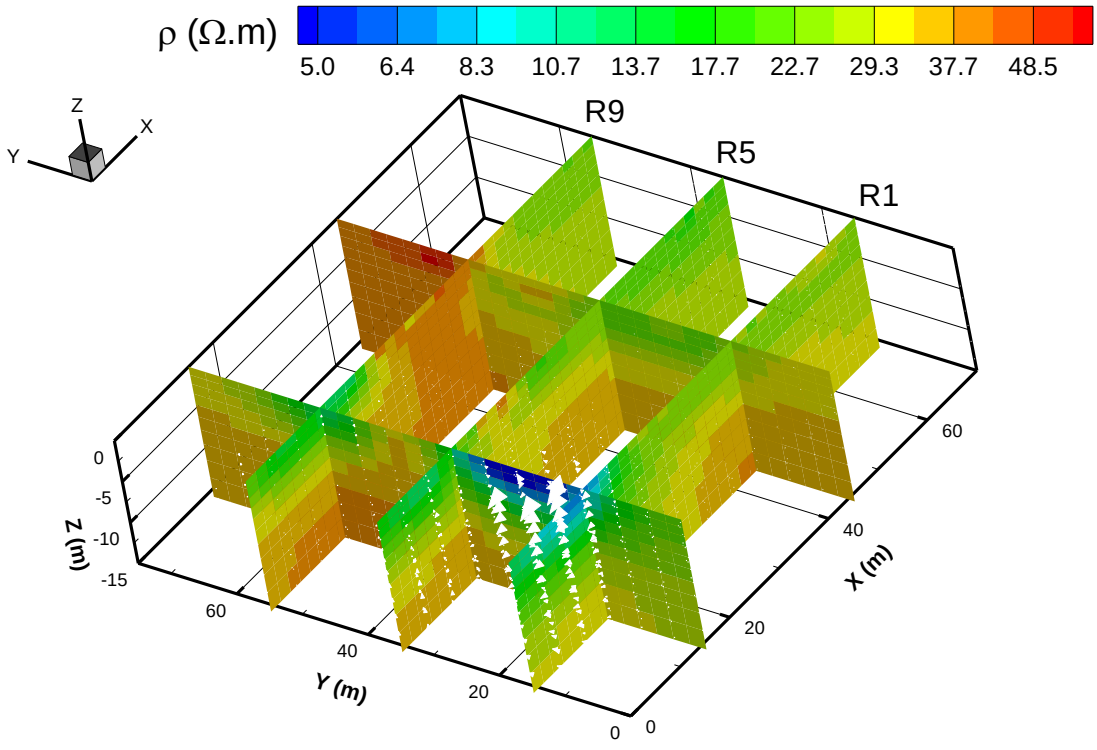

Figure 16. Estimated source current density vectors superimposed on the electrical resistivity tomograms. Note that the source current density is approximately co-located with the bottom of the high electrical conductivity anomaly.

Highlights

1. Self-potential tomography is used to monitor a sandbox experiment

2. This method can be used in real time to localize the position of the advecting plume

3. This method is proved to be efficient in field condition to localize contaminant plumes